Joule

CellPress

Article

# Printable, emissivity-adaptive and albedo-optimized covering for year-round energy saving

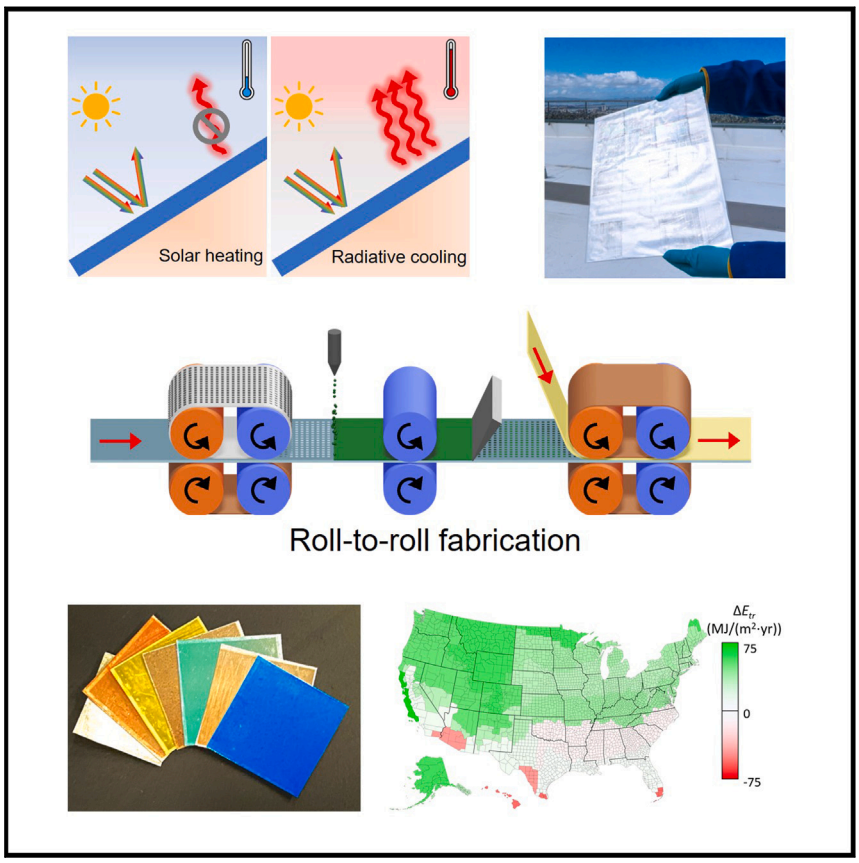


Temperature-adaptive radiative cooling materials overcome the overcooling problem of daytime radiative coolers by automatically switching their thermal emissivity in response to surface temperature. However, practical applications of these materials are limited. As a solution, we adopt a new optical structure with a temperature-adaptive material to enable roll-to-roll fabrication at low cost. Such a structure also features optimizable solar reflection, showing great potential in energy saving and thermal comfort in various climates.

Jiachen Li, Kaichen Dong, Tiancheng Zhang, ..., Ali Javey, Jie Yao, Junqiao Wu

wuj@berkeley.edu

## Highlights

A smart radiative cooling structure that is roll-to-roll fabricated at low cost

Optimized albedo for aesthetic needs and energy saving

Optical antenna array structure for lifetime robustness

Thermal regulation performance validated by experiments and numerical simulations

Li et al., Joule 7, 1–16
November 15, 2023 
https://doi.org/10.1016/j.joule.2023.09.011

Please cite this article in press as: Li et al., Printable, emissivity-adaptive and albedo-optimized covering for year-round energy saving, Joule (2023), https://doi.org/10.1016/j.joule.2023.09.011

Joule

CellPress

Article

# Printable, emissivity-adaptive and albedo-optimized covering for year-round energy saving

Jiachen Li,[1,2,3,11] Kaichen Dong,[1,4,5,6,11] Tiancheng Zhang,[1,2,3] Derick Tseng,[1] Cheng Fang,[1] Ruihan Guo,[1,2] Jingang Li,[7] Yujie Xu,[8] Chaochao Dun,[9] Jeffrey J. Urban,[9] Tianzhen Hong,[8] Costas P. Grigoropoulos,[7] Ali Javey,[2,10] Jie Yao,[1,2,3] and Junqiao Wu[1,2,3,12,*]

## SUMMARY

**Radiative cooling uses high-emissivity materials to passively cool the surface of outdoor objects, such as building roofs on hot days. The issue of overcooling with this technology on cold days can be addressed by structures with thermal emissivity that is adaptive to temperature. Despite recent advances in temperature-adaptive structures, great challenges remain in their fabrication feasibility and unoptimized solar heating that may override the radiative cooling benefit. In this work, we develop a printable, emissivity-adaptive and albedo-optimized covering (PEAC) based on recyclable materials with roll-to-roll fabrication. A PEAC automatically switches its sky-window emissivity from 0.25 to 0.85 when the surface temperature exceeds a pre-set transition temperature, delivering an albedo optimized for maximal year-round energy saving or thermal comfort in a given climate.**

## INTRODUCTION

The global demand for energy-efficient and sustainable temperature regulation solutions has been rapidly rising, driven by factors such as the energy crisis, climate change, and urbanization. As an attractive alternative or add-on to conventional heating, ventilation, and air conditioning (HVAC) systems, radiative cooling has been extensively studied over the past few decades with wide application and commercialization.[1–13] It is based on the radiative emission of heat from terrestrial objects to outer space through the mid-infrared (IR) atmospheric transparency window, known as the "sky window," ranging from 8 to 14 μm. Therefore, radiative cooling can efficiently reduce the temperature of, e.g., buildings,[1] vehicles,[2,3] human bodies,[4] and other objects without the need for external power sources or refrigerants. To radiate heat efficiently, passive radiative cooling materials are typically designed to have minimum absorptance in the solar wavelength range (0.3–2.5 μm) and maximum emissivity in the sky window. Such a property has been realized in various materials such as wood,[5] paints,[6–8] fabrics,[9,10] and dielectrics.[11,12] However, due to their static optical properties, most passive radiative cooling materials continue to radiate heat off objects even at ambient temperatures below the desired temperature, resulting in the unwanted overcooling of the objects in areas with large seasonal or daily temperature variations.[13] Since overcooling leads to discomfort as well as the need for additional energy for space heating, circumventing or alleviating the overcooling problem remains a significant challenge for the widespread implementation of radiative cooling technologies.

## CONTEXT & SCALE

Temperature-adaptive passive radiative cooling materials and structures provide a promising solution to the well-known overcooling problem of daytime radiative coolers through their automatic switching between a radiative cooling mode and a heat retaining mode. However, considerable obstacles persist in their practical fabrication. In addition, the effect of unoptimized solar heating may outweigh the benefits of radiative cooling.

This work demonstrates a printable, emissivity-adaptive and albedo-optimized covering (PEAC) crafted from recyclable materials and fabricated using a roll-to-roll process. A PEAC automatically switches its sky-window emissivity from 0.25 to 0.85 when the surface temperature surpasses a predefined transition temperature. Moreover, the albedo of a PEAC can be optimized to maximize energy saving throughout the year or enhance thermal comfort, customized based on the local climate.

Please cite this article in press as: Li et al., Printable, emissivity-adaptive and albedo-optimized covering for year-round energy saving, Joule (2023), https://doi.org/10.1016/j.joule.2023.09.011



A range of temperature-adaptive technologies have been developed to mitigate the overcooling at low temperatures, including electrical dynamic glazing,[14,15] mechanical-driven structures,[16,17] and temperature-activated bimorph-based structures.[18] The requirements of external energy input or moving parts severely limit their energy efficiency and lifetime. Very recently, vanadium dioxide ($VO_2$) based Fabry-Perot (FP) resonators were realized to achieve self-switching in thermal radiation while avoiding those drawbacks.[19–21] However, the scalability and performance of these $VO_2$-based FP resonators are still restricted due to several factors. First, bounded by the FP resonance mechanism, the emissivity of these devices depends sensitively on the uniformity of the dielectric spacer thickness, leading to limited upgradability and increased difficulty for mass production. Second, the $VO_2$-based FP resonators are produced with expensive materials or fabrication methods that restrict their size and cost effectiveness for scale applications. Last, the albedo of the structure is an equally important factor for the energy balance, which needs to be independently optimized for maximum energy saving in a given climate.

Here, we present a printable, emissivity-adaptive and albedo-optimized covering (PEAC) as the solution (Table S1). This flexible covering is made through a roll-to-roll fabrication process using tungsten-doped $VO_2$ ($W_xV_{1-x}O_2$) particles and inexpensive recyclable materials. As a temperature-adaptive radiative cooling structure, a PEAC automatically switches the sky-window emissivity ($\varepsilon_{sky}$) from ~0.25 to ~0.85 when the surface temperature rises across a pre-set transition temperature (Figure 1A). This emissivity switching is enabled by in-plane inter-block photonic resonance instead of cross-plane FP resonance; hence, the performance of a PEAC is independent of the thickness of the dielectric layer in the structure, enabling roll-to-roll fabrication (Figure 1B). Moreover, to maximize annual energy saving in different climates, a PEAC can be customized with mid-IR transparent pigments to achieve optimal albedo as well as different visual colors (Figure 1C). Both rooftop and indoor temperature regulation of a PEAC were demonstrated in field experiments. Numerical simulations with a climate database further demonstrate the energy-saving potential of a PEAC across various climate zones in the US (Figure 1E).

## RESULTS AND DISCUSSION

### PEAC design and fabrication

The PEAC functions as a radiative cooler only when the surface temperature ($T_s$) is high (Figure 1A). Such temperature-adaptive thermal emission is based on a unique photonic structure and the metal insulator transition (MIT) of $VO_2$.[22–24] As shown in Figure 2A and S5, the PEAC consists of a polyester (PET) substrate, an aluminum (Al) layer, a periodic array of $W_xV_{1-x}O_2$ blocks, and a polyethylene (PE) overlayer. The $W_xV_{1-x}O_2$ block array is carefully designed with the guidance of numerical electromagnetic simulations while considering the fabrication feasibility and cost. The phase transition temperature ($T_{MIT}$) of $VO_2$ is approximately 68°C, which can be reduced by W doping to fit multiple applications (Figure S8). For instance, with 2% of W doping in $VO_2$, the corresponding $T_{MIT}$ is about 20°C, suitable for household thermal regulation[25,26]. It is worth noting that a PEAC is highly durable since $W_xV_{1-x}O_2$ is protected from air and water due to the PE sealing (Figure S4 and S9). Furthermore, the materials used, such as PE, PET, and Al, are all sustainable and recyclable,[27] resulting in a low lab cost of ~$1/sqft (Table S2).

We have developed a roll-to-roll printing process for the mass production of PEACs, as illustrated in Figure 2A and S1. Initially, the PE film is thermally micro-imprinted by a reusable metal template through a heated roller system. The reusable template is a

[1]Department of Materials Science and Engineering, University of California, Berkeley, CA 94720, USA

[2]Materials Sciences Division, Lawrence Berkeley National Laboratory, Berkeley, CA 94720, USA

[3]Applied Science and Technology Graduate Group, University of California, Berkeley, CA 94720, USA

[4]Tsinghua-Berkeley Shenzhen Institute, Tsinghua Shenzhen International Graduate School, Tsinghua University, Shenzhen, Guangdong 518055, China

[5]Institute of Data and Information, Tsinghua Shenzhen International Graduate School, Tsinghua University, Shenzhen, Guangdong 518055, China

[6]Center of Double Helix, Tsinghua Shenzhen International Graduate School, Tsinghua University, Shenzhen, Guangdong 518055, China

[7]Department of Mechanical Engineering, University of California, Berkeley, CA 94720, USA

[8]Building Technology and Urban Systems Division, Lawrence Berkeley National Laboratory, Berkeley, CA 94720, USA

[9]The Molecular Foundry, Lawrence Berkeley National Laboratory, Berkeley, CA 94720, USA

[10]Department of Electrical Engineering and Computer Sciences, University of California, Berkeley, CA 94720, USA

[11]These authors contributed equally

[12]Lead contact

*Correspondence: wuj@berkeley.edu

https://doi.org/10.1016/j.joule.2023.09.011

Please cite this article in press as: Li et al., Printable, emissivity-adaptive and albedo-optimized covering for year-round energy saving, Joule (2023), https://doi.org/10.1016/j.joule.2023.09.011





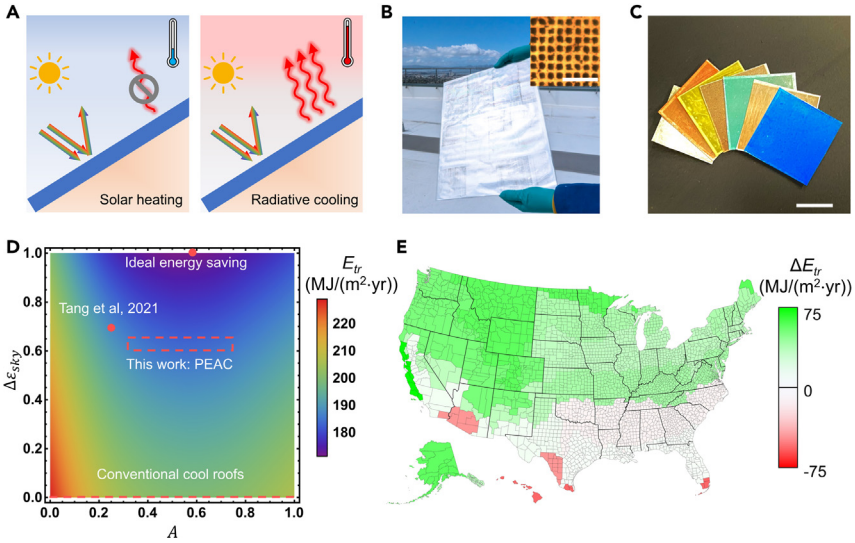


**Figure 1. PEAC and its energy-saving potential**

(A) Schematic of household thermal regulation with a PEAC roof.

(B) A photo of a 30 cm by 40 cm roll-to-roll manufactured PEAC. Inset: an optical microscopic image of the PEAC structure. Scale bar: 20 μm.

(C) PEACs colorized with infrared transparent pigments. Scale bar: 1 cm.

(D) Simulated thermal regulation energy consumption ($E_{tr}$) to keep the indoor temperature of a single house between 22°C and 24°C in Seattle, Washington. $\Delta\varepsilon_{sky}$ is the tuning range of the emissivity (the emissivity difference between the high-temperature state and the low-temperature state) of a covering, and $A$ is solar absorptance. The ideal point and the work published in Tang et al.[19] are also noted.

(E) Map of the energy saving ($\Delta E_{tr}$) across the 15 climate zones in the US by using a PEAC in place of a conventional cool roof ($A$ = 0.05 and $\varepsilon_{sky}$ = 0.95).

metal sheet with a periodic array of micron-sized pillars constructed on the surface (Figure S2 and S3). When the surface of the PE film is heated above 110°C, an array of pockets with identical dimensions are imprinted on the surface of the PE. Considering the heat capacity of the PE film, the temperature setpoint ($T_{set}$) of the rollers should increase with imprinting speed. We have achieved an imprinting speed that is approximately 100 m per hour at $T_{set}$ = 150°C. Subsequently, commercial $W_xV_{1-x}O_2$ nanoparticles are dispersed onto the patterned PE film surface by spraying a mixture of $W_xV_{1-x}O_2$ particles suspended in isopropyl alcohol. After mechanical pressing and surface cleaning, a PE film embedded with a planar array of $W_xV_{1-x}O_2$ blocks is produced. Finally, the PEAC is formed by laminating the patterned side of the PE/$W_xV_{1-x}O_2$ film onto a pre-metallized PET substrate via running it through another heated roller system. The entire fabrication process does not involve lithography or vacuum techniques; hence, it is scalable for mass production.

## Mechanism of a PEAC

The spectral thermal emissivity and solar absorptance of PEACs were accurately determined through spectroscopy measurements. The spectral reflectance of PEACs, $r(\lambda, T)$, was measured by an ultraviolet-visible and near-infrared (UV-vis-NIR) spectrometer equipped with an integrating sphere and a Fourier transform infrared (FTIR) spectrometer. Since PEACs have zero transmittance to light, the spectral thermal emissivity, $\varepsilon(\lambda, T)$, and spectral solar absorptance, $a(\lambda, T)$, were calculated by $1 - r(\lambda, T)$ in the mid-IR and UV-vis-NIR range, respectively. As depicted in Figure 2B, the thermal emissivity of a PEAC exhibits a significant boost from low

Please cite this article in press as: Li et al., Printable, emissivity-adaptive and albedo-optimized covering for year-round energy saving, Joule (2023), https://doi.org/10.1016/j.joule.2023.09.011



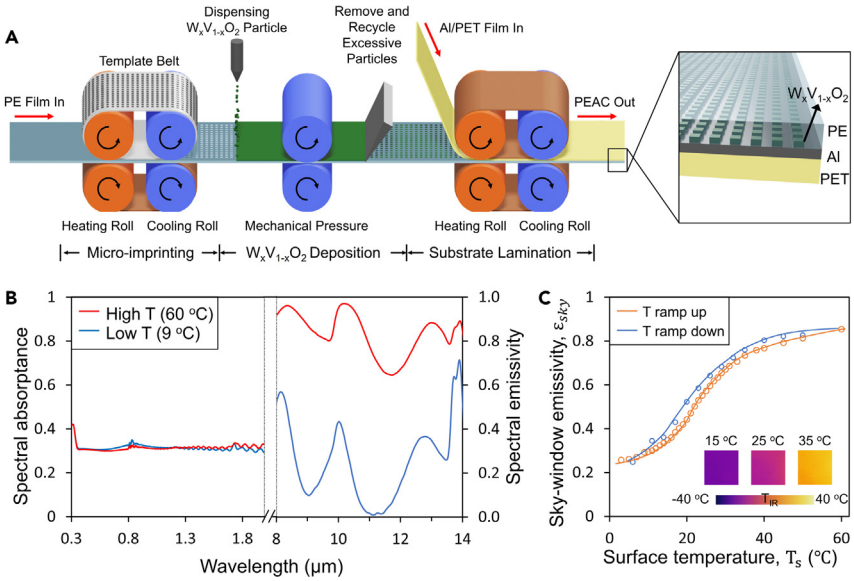


**Figure 2. Fabrication process and spectral properties of a PEAC**

(A) Roll-to-roll printing process to manufacture a PEAC. Orange and blue rollers are at 110°C and room temperature, respectively.

(B) Spectrally resolved solar absorption and thermal emissivity of a PEAC.

(C) Sky-window emissivity by integrating the measured spectral emissivity in the sky window. Inset: thermal images of a PEAC taken at three different actual temperatures. $T_{IR}$ is the temperature readout of the thermal camera.

to high values when the temperature increases beyond the $T_{MIT}$ of $W_xV_{1-x}O_2$, whereas the solar absorptance (A) of the PEAC remains unchanged. To quantify the emissivity switching, $\varepsilon_{sky}$ of a PEAC is calculated from $\varepsilon_{sky}(T) = \frac{\int \varepsilon(\lambda,T)B(\lambda,T)\,d\lambda}{\int B(\lambda,T)\,d\lambda}$, where the integration range is from 8 to 14 μm (sky window), and $B(\lambda, T)$ is the spectral intensity of blackbody radiation at temperature $T$. As shown in Figure 2C, $\varepsilon_{sky}$ of a PEAC switches from 0.25 to 0.85 over a typical roof temperature range.

The emissivity switching was investigated via finite element simulation. When the $T$ is below $T_{MIT}$, the $W_xV_{1-x}O_2$ blocks are in the insulating state and thus largely transparent to IR radiation in the sky window.[28] As a result, most of the IR radiation is reflected by the Al layer underneath the $W_xV_{1-x}O_2$ blocks, resulting in a low absorptance/emissivity. However, at higher temperatures ($T > T_{MIT}$), $W_xV_{1-x}O_2$ switches to the metallic state with a large imaginary part of permittivity in the mid-IR. The mid-IR electromagnetic fields will be "funneled" into the gaps between neighboring $W_xV_{1-x}O_2$ blocks due to a large impedance mismatch between the $W_xV_{1-x}O_2$ blocks and the surrounding PE matrix. Hence, two neighboring $W_xV_{1-x}O_2$ blocks will form an optical antenna,[29] and the electric field intensity at their surface is drastically enhanced, generating strong evanescent waves to be absorbed in the metallic $W_xV_{1-x}O_2$ blocks (Figure 3B). Consequently, the PEAC structure consisting of periodic $W_xV_{1-x}O_2$ blocks becomes an array of high-loss optical antennas, giving rise to high absorptance in the mid-IR (Figure 3C). According to Kirchhoff's law of radiation,[30] the emissivity also switches from low to high values when the temperature rises across $T_{MIT}$. The high emissivity of PEACs at $T > T_{MIT}$ relies solely on the periodic array of the $W_xV_{1-x}O_2$ blocks and is independent of the thickness of the PE layer that merely acts as a protective encapsulation instead of an FP cavity spacer. This is further proved by both experiments and simulations in which the general line shape

Please cite this article in press as: Li et al., Printable, emissivity-adaptive and albedo-optimized covering for year-round energy saving, Joule (2023), https://doi.org/10.1016/j.joule.2023.09.011





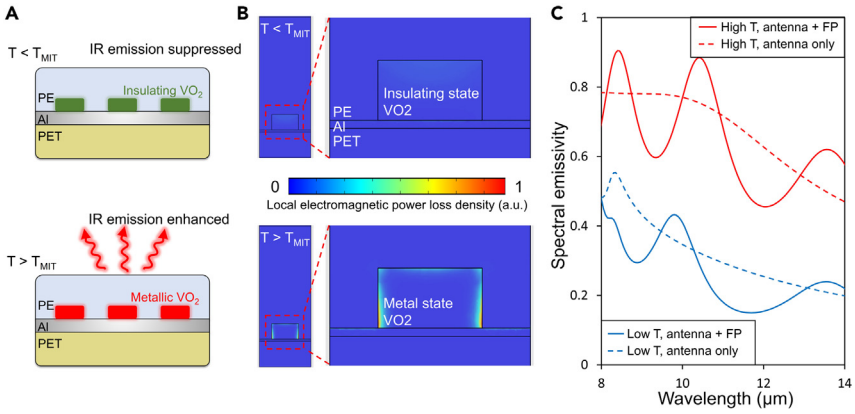


**Figure 3. The working mechanism of a PEAC**

(A) A schematic showing the in-plane photonic resonance mechanism of a PEAC.

(B) Whole-unit cell view (left) and zoom-in view (right) of the mid-IR absorption profile in a PEAC at both low and high temperatures. The wavelength of incident light is 12 μm.

(C) Numerically calculated mid-IR absorption/emissivity, showing that the emissivity switch of a PEAC is dominated by the antenna mechanism. The dashed curves show the antenna-only scenario in which the PE thickness is made infinite to eliminate the Fabry-Perot cavity.

of the absorptance spectrum remains the same with the change in PE layer thickness, as shown in Figure S10 and S11. Note that since the antenna absorptance does not depend on optical resonance at specific wavelengths, this switch in emissivity still exists even outside the sky window spectral range, benefiting applications in outer space[29] (Figure S6). Simulations prove the emissivity switching even at infinite PE thickness; hence, the performance does not rely on a cross-plane FP resonance (Figure 3C). Such tolerance to layer thickness variation greatly eases the fabrication process and opens the possibility of stacking or adding new functionality along the cross-plane direction, as shown below.

## Pigment-aided albedo optimization

For real-world applications to fit different climates, albedo is an important factor, since the heating from solar radiation, if not managed well, would easily offset the effect of radiative cooling (Figure 5D and S19). With optimization of albedo, the year-round energy saving of a PEAC in various climates can be greatly improved.[31–34] The albedo optimization of a PEAC is enabled by adding a layer of pigments that are selectively absorptive in the solar range yet transparent in the mid-IR range. As shown in Figure 4A, the pigments can be dispersed onto the PEAC surface and then sealed with another layer of PE film. Due to the dominance of inter-block photonic resonance, the addition of pigments and the sealing PE layer affects only the position of the FP peaks and not the broadband trend in emissivity switching. This allows us to modify the solar reflectance (hence solar heating and visual color) without sacrificing the thermal emission switching in the sky window. By using $BaF_2$ (white), ZnSe (yellow), $Fe_2O_3$ (red), Prussian Blue (blue), and their combinations, we are able to broadly tune the color and solar absorptance of a PEAC (Figure 4B and 1C). The colored PEACs also raise commercialization potential for aesthetic reasons.

The solar absorption spectra of the colored PEACs are shown in Figure 4C. The pigments tune the absorption of PEACs primarily in the visible range. Note that although different pigments have absorption peaks at different wavelengths, it is possible to have broadband absorption in the visible range with combinations of

Please cite this article in press as: Li et al., Printable, emissivity-adaptive and albedo-optimized covering for year-round energy saving, Joule (2023), https://doi.org/10.1016/j.joule.2023.09.011



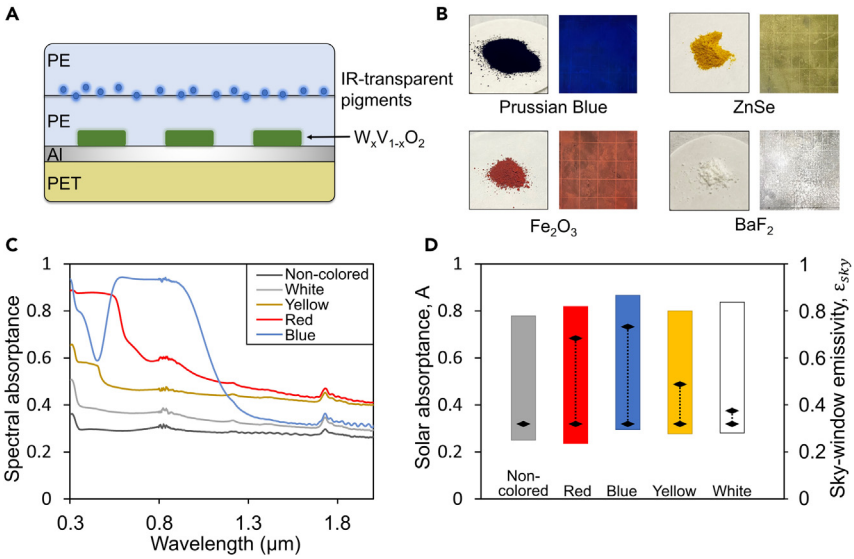


**Figure 4. Albedo optimization and colorization of a PEAC**

(A) Cross-section schematic of a colored PEAC.

(B) Photos of pigments and corresponding images of colored PEACs.

(C) Spectrally resolved solar absorptance of colored PEACs.

(D) Integral solar absorptance and sky-window emissivity of colored PEACs. The color bars show the range of temperature-adaptive sky-window emissivity (right axis) for the corresponding colored PEAC. The diamond markers show the solar absorptance (left axis) of each, and the dotted lines show the ranges of solar absorptance that can be tuned with the coverage of pigments.

different pigments. The mid-IR spectral emissivity of the colored PEACs at both low and high temperatures was measured by FTIR spectroscopy (Figure S12), showing an evident insensitivity to the pigments added. $\varepsilon_{sky}$ was calculated and shown in Figure 4D.

## Thermal regulation and energy-saving performance of a PEAC

Outdoor temperature regulation experiments were conducted to test the performance of a PEAC as a roof coating. A PEAC, a commercial dark roof coating product (BEHR #N520 Asphalt Gray), and a cool roof coating product (Henry Enviro-White Extreme Elastomeric Roof Coating) were used as roofs on three mock-up model houses (Figure S15). The model houses were 3D printed with acrylonitrile butadiene styrene (ABS) filaments and painted with white (walls) and dark (windows and doors) commercial paints.[35] To best simulate the heat exchange in real houses, the thermal resistance per area of the model house was carefully tuned to be close to that of real houses by adjusting the 3D printing filling ratio and thickness of the walls and roofs.[36,37] The experiments were performed on cloudless summer days on a residential house roof in Berkeley, California (Figure 5A), and the real-time weather data were retrieved from a weather station near the experiment site.

The 24 h record of the indoor temperature is shown in the middle panel of Figure 5B, whereas the left and right panels are zoom-in plots at cold night and hot noon, respectively. The temperature-time series show that during the night, the PEAC roof keeps the indoor temperature ~2°C higher than the other two roof materials, indicating that the PEAC has switched to a low-emissivity, heat-retaining mode. In contrast, at noon under direct sunlight, the PEAC performs as a cool roof, delivering a cooler indoor temperature than the commercial dark roof, although with a slightly higher temperature than that under the commercial cool roof. It is known that the

Please cite this article in press as: Li et al., Printable, emissivity-adaptive and albedo-optimized covering for year-round energy saving, Joule (2023), https://doi.org/10.1016/j.joule.2023.09.011





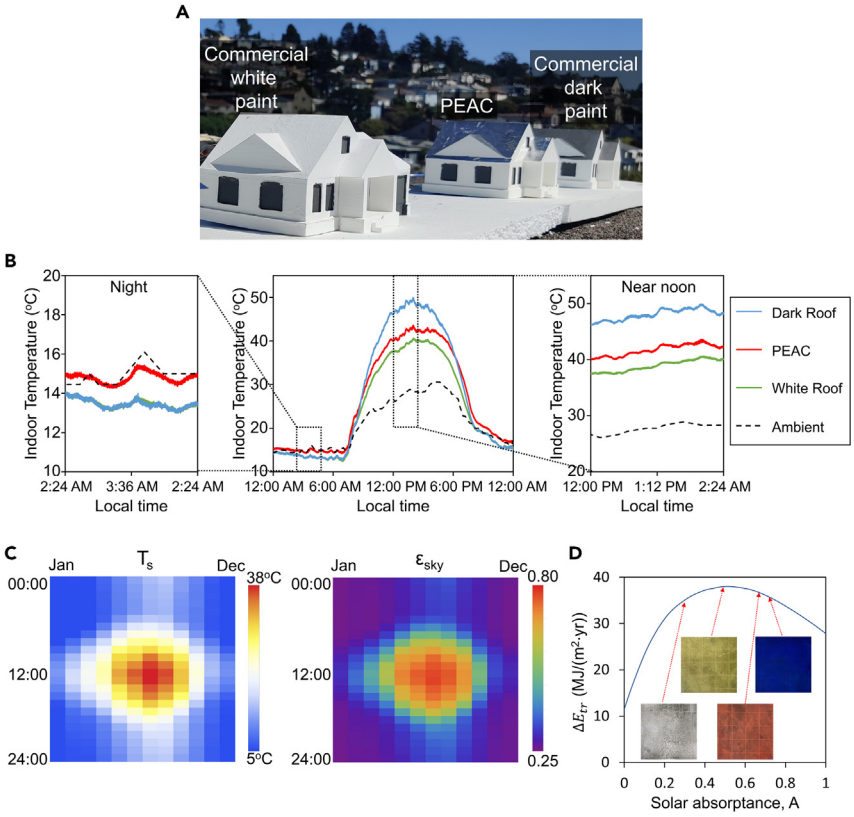


**Figure 5. Outdoor performance of a PEAC**

(A) Setup of the outdoor experiments.

(B) 24 h recorded indoor temperature of the model houses covered with different roof materials. Left and right panels are scaled views of night and near noon, respectively. See also Figure S16

(C) Equilibrium surface temperature ($T_s$) and designed sky-window emissivity ($\varepsilon_{sky}$) of a PEAC over the year.

(D) Extra energy-saving ($\Delta E_{tr}$) plot for a house equipped with colored PEACs in place of a cool roof material ($A$ = 0.05 and $\varepsilon_{sky}$ = 0.95) in Seattle, Washington.

coefficient of performance (COP) of space heaters is generally much lower than air conditioners, and space heaters consume more energy annually.[38,39] Therefore, in this one-spot summer experiment, the better nighttime performance of the PEAC over conventional cool roofs would indeed outweigh, in terms of overall energy saving, its worse cooling power at daytime. From simulations considering typical house structures and COPs, the experimental temperature difference between a PEAC and a commercial white cool roof would lead to 78.61 kJ/m$^2$ energy saving over 24 h (details in experimental procedures). Other seasons have lower average temperatures than summer; hence, space heating takes larger portions in energy consumption, and a PEAC would deliver better energy performance in other seasons than conventional cool roofs under the same HVAC system strategy. As a result, a PEAC is expected to outperform commercial cool roofs in terms of year-round energy saving due to its around-the-clock, all-season thermal regulation. Moreover, the roof temperature records (Figure S17) show that the temperature of the PEAC remains above the dew point over the 24 h period, while the other roofing materials are all cooled to the dew point temperature at night. Thus, a PEAC is also effective in mitigating the well-known condensation problem of cool roofs.[40,41] In energy-poverty areas or scenarios where heating and air conditioning are not available

Please cite this article in press as: Li et al., Printable, emissivity-adaptive and albedo-optimized covering for year-round energy saving, Joule (2023), https://doi.org/10.1016/j.joule.2023.09.011



(e.g., tents or power outrage times), a PEAC would also reduce occupants' thermal discomfort because it cuts down the daily or seasonal temperature swing toward the pre-set, constant $T_{MIT}$ during free-floating seasons or in energy poverty areas (Figure S20).

We further analyzed the general performance of a PEAC in household energy saving with numerical simulations. To estimate the energy saving of a roof material, we first calculated the hour-month map of equilibrium roof surface temperature ($T_s$) with TMY3 weather files included in the EnergyPlus climate database.[42] The result of using a PEAC roof in Seattle, Washington is shown in Figure 5C. We assumed that the building requires heating when $T_s$ is lower than a heating setpoint, $T_{h,set}$ (22°C), and needs cooling when $T_s$ is higher than a cooling setpoint, $T_{c,set}$ (24°C).[19] The heating/cooling efficiency of houses in different cities in the US was extracted from past simulation results of cool roof energy savings to determine the total thermal regulation energy ($E_{tr}$) required to keep the building temperature between $T_{h,set}$ and $T_{c,set}$[19,43]. We define energy saving ($\Delta E_{tr}$) as the difference between $E_{tr}$ of a PEAC and $E_{tr}$ of a representative cool roof material (fixed solar absorptance $A$ = 0.05 and fixed $\varepsilon_{sky}$ = 0.95), where a positive value of $\Delta E_{tr}$ indicates that a PEAC is more energy efficient. Therefore, $\Delta E_{tr}$ serves as a figure of merit of the energy-saving potential for a roof material. Figure 5D shows the dependence of $E_{tr}$ on solar absorption for the colored PEACs, which proves again the importance of optimizing the albedo of a radiative cooling roof. As shown in Figure S19, the maximum total energy saving originates from the balance between solar heating and daytime radiative cooling with an optimal $A$ that varies with different climate zones (Table S3). The simulated $\Delta E_{tr}$ for houses built before 1980 in cities representing the 15 US climate zones were illustrated in Figure 1E, showing that a PEAC is more energy efficient than conventional cool roofs in household temperature regulation in 12 of the 15 climate zones. For example, a PEAC roof with an area of 1700 sqft (158 $m^2$) will save 12.63 GJ of energy each year for a typical single-family house built before 1980 in San Francisco, California. This is equivalent to the elimination of 2,486 kg of carbon dioxide emission.[44] Further simulations predict that a PEAC would outperform the conventional cool roof in all 15 climate zones if its albedo can be tuned to a wider range of values (Figure S18).

## Conclusions

We have developed a PEAC that is roll-to-roll fabricated using recyclable materials. The roll-to-roll fabrication is enabled by the unique, cavity-free structure of the PEAC, which eliminates the sensitive thickness dependence in previous temperature-adaptive radiative structures. Outdoor experiments and numerical simulations demonstrate PEAC's excellent temperature regulation and energy-saving potentials enabled by the automatic switching between the radiative-cooling mode and the heat-retaining mode. The PEAC opens the possibility for large-scale applications of temperature-adaptive radiative coatings with aesthetic benefits. Buildings with a PEAC applied to the envelope will be more thermally resilient during extreme hot or cold days coincident with power outages. Additionally, our simulation analysis on albedo-optimized temperature-adaptive radiative coolers can also serve as a guidance to future research for dynamic radiative coolers.

In the future, the emissivity switching would be made sharper if $W_xV_{1-x}O_2$ particles with higher quality could be used.[45,46] Machine-learning-guided electromagnetic simulations on more complex photonic structures would further boost the performance of a PEAC with reduced low-temperature emissivity and a wider solar absorption range. Extension from roof application to wall application could be enabled by

Please cite this article in press as: Li et al., Printable, emissivity-adaptive and albedo-optimized covering for year-round energy saving, Joule (2023), https://doi.org/10.1016/j.joule.2023.09.011





directional-emission photonic structures, which would bring further prospects in building energy saving.[47]

A PEAC can also be applied to objects beyond building roofs and walls, such as space objects, tents, and vehicles. Since a PEAC switches emissivity in broadband thanks to the optical antenna design, it is ideal for outer space applications where the sky window is absent.[48] For heavy-duty applications such as tents and vehicle wraps, the mechanical strength of a PEAC could be further enhanced by adding more supporting layers such as polyimide and Kevlar. The durability of a PEAC can also be improved with the typical stitching method used in space multi-layer insulations.[49,50] As a PEAC is free of a cavity layer and operates based only on in-plane photonic resonance, the pattern of a PEAC can be imprinted onto a wide variety of polymer products, including plastic shingles and containers. Moreover, by replacing the Al layer with transparent conducting oxides, an optically transparent PEAC could also be fabricated, which may find applications in window coating or greenhouse covering.

## EXPERIMENTAL PROCEDURES

### Resource availability

#### *Lead contact*

Further information and requests for resources and materials should be directed to and will be fulfilled by the lead contact, Junqiao Wu (wuj@berkeley.edu).

#### *Materials availability*

This study did not generate new unique materials.

#### *Data and code availability*

All data required to evaluate the conclusions in the manuscript are available in the main text or the supplemental information.

### Preparation of a PEAC

Commercial PE food wrap (Saran Premium Wrap, S. C. Johnson & Son) was first imprinted by passing through a laminator (ProLam Ultra-X Series Akiles Model X10) equipped with a nickel (Ni) template that has micron-sized pillar patterns on it. The laminator consists of four pairs of rollers, three of them are heated to a preset temperature and the last pair of rollers are at room temperature. After the imprinting process, a mixture of isopropanol and sub-micron $W_xV_{1-x}O_2$ particles (Hongwu International Group Ltd., size further reduced by 3 h of high-energy ball milling) were spread onto the patterned PE film with an airbrush. The surface of the film was cleaned by Texwipe, resulting in an array of $W_xV_{1-x}O_2$ blocks in the PE film. The PE film with $W_xV_{1-x}O_2$ block array was laminated to an Al foil (Rhino Aluminum) or an Al/PET film (McMaster-Carr) at the same temperature as that of the imprinting step to form the plain (non-colored) PEAC. The colored PEAC was prepared with two more steps: infrared-transparent pigments were first sprayed onto the non-colored PEAC surface. Subsequently, another layer of PE film was laminated on top to seal the pigments (Figure S1). When a PEAC is placed under a light source, both specular reflection and diffraction grating colors are visible due to the dominant reflection by the Al surface as well as scattering by the $W_xV_{1-x}O_2$ periodic structure.

The nickel template used in the imprinting process was fabricated as follows: The pre-designed inverse pattern, i.e., an array of holes, was created on a 675 μm thick Si wafer by standard photolithography and ICP etching. A thin layer of Cr was

Please cite this article in press as: Li et al., Printable, emissivity-adaptive and albedo-optimized covering for year-round energy saving, Joule (2023), https://doi.org/10.1016/j.joule.2023.09.011



subsequently sputtered onto the patterned Si wafer as the seed layer. Then 20 μm-thick Ni was deposited onto the metallized Si wafer by electroplating. After soaking in 20% KOH solution, the Ni layer will be separated from the Si surface, forming a freestanding template (Figure S2). In order to integrate the Ni template with the laminator, the Ni template was attached to a polyimide film (McMaster-Carr) and then wrapped onto the rollers during mass production.

### Spectrally resolved measurements

Thermal spectral reflectance at normal incidence, denoted as $r(\lambda, T)$, was characterized by a Nicolet iS50 FTIR spectrometer and Nicolet Continuum microscope over the 8–14 μm wavelength range. A blade aperture of 100 × 100 μm was used to select the area of interest. All reflection spectra were normalized to the reflection spectrum of a 400 nm-thick aluminum film. The temperature of the samples, ranging from 3°C to 60°C, was controlled by a dry ice cooled closed-loop thermal stage, connected to a Lakeshore 321 temperature controller. According to Kirchhoff's law of radiation, in a state of thermodynamic equilibrium, the spectral emissivity $\varepsilon(\lambda, T)$ is equal to the spectral absorptance $a(\lambda, T)$. Considering that a PEAC comprises a thick aluminum layer, its transmittance in both the solar and thermal infrared wavelength ranges was considered to be zero. Thus, its thermal spectral emissivity in this range was computed as $\varepsilon(\lambda, T) = a(\lambda, T) = 1 - r(\lambda, T)$. Near-normal-hemispherical solar spectral reflectance, $r(\lambda)$, was measured from 300 nm to 2,500 nm with an Agilent Cary 5000 UV-vis-NIR spectrometer equipped with an Internal Diffuse Reflectance Accessory (DRA-2500), which captures both specular and diffuse reflections. Solar spectral absorptance was also computed as $a(\lambda) = 1 - r(\lambda)$, since a PEAC is essentially opaque to sunlight.

The solar absorptance $A$ and sky-window thermal emissivity $\varepsilon_{sky}$ can be calculated from the corresponding spectral data using the following formulas:

$$A = \left(\int_{0.3\ \mu m}^{2.5\ \mu m} I_s(\lambda)\, a(\lambda)\, d\lambda\right) \Big/ \left(\int_{0.3\ \mu m}^{2.5\ \mu m} I_s(\lambda)\, d\lambda\right) \quad (1)$$

$$\varepsilon_{sky}(T) = \left(\int_{8\ \mu m}^{14\ \mu m} B(\lambda)\, \varepsilon(\lambda, T)\, d\lambda\right) \Big/ \left(\int_{8\ \mu m}^{14\ \mu m} B(\lambda)\, d\lambda\right) \quad (2)$$

where $I_s(\lambda)$ is the spectral solar radiance, and B(λ) is the spectral intensity of blackbody emission.

### Thermal infrared imaging and analysis

Thermal infrared images were acquired using an FLIR ONE infrared camera operating within the sky window wavelength range. To mitigate reflections from the camera and the surroundings, the default viewing angle was set as 20° instead of the normal incident direction. Additionally, a cryogen-cooled high emissivity plate was employed as the background.

During the capture of thermal infrared images, the camera measures the incident thermal infrared radiation and provides temperature readouts ($T_{IR}$) assuming a constant thermal emissivity (0.90) for the target. For a surface with a constant thermal emissivity, the $T_{IR}$ vs. $T_s$ relationship should exhibit approximately linear behavior. Consequently, the presence of a step feature in the $T_{IR}$ vs. $T_s$ curve signifies a transition in the emissivity of the PEAC (Figure S8).

To justify that the emissivity-switching performance of a PEAC is insensitive to angles, the angular dependence of the emissivity of a PEAC at both high and low

Please cite this article in press as: Li et al., Printable, emissivity-adaptive and albedo-optimized covering for year-round energy saving, Joule (2023), https://doi.org/10.1016/j.joule.2023.09.011





temperature (Figure S7) was experimentally measured. An IR camera was used to read $T_{IR}$ of the same spot on a PEAC from different angles, which directly related to the power of thermal radiation.[51] Note that the measurement starts from $\theta \approx 20^{\circ}$ to avoid unwanted reflectance of IR power radiated from the IR camera itself. As shown in Figure S7B, the $T_{IR}$ of a PEAC remains almost unchanged at angles from 20° to 70° in both low-temperature and high-temperature states, indicating that the emissivity of a PEAC is angle insensitive, which is ideal for thermal regulation applications[52]

## Durability test

To evaluate the durability of a PEAC toward the day-to-night temperature cycles, we use a customized durability test system, which consists of an Arduino board (Mega 2560), a switch module (XY-GMOS), a DC power supply (Agilent 6645A), and a heating stage. The temperature of the heating stage is set to switch across the phase transition temperature (from 21°C to 70°C) of $W_xV_{1-x}O_2$ for a given number of cycles. A piece of a PEAC sample was attached to the heating stage and the thermal emissivity was measured after 1, 10, 100 and 1000 cycles, respectively (Figure S9). We did not observe any delamination of the PEAC sample during this experiment, proving good mechanical stability during thermal cycling tests.

## Simulation of device properties

The spectral absorptance of a PEAC is numerically calculated using COMSOL Multiphysics, with all the geometric parameters matching the original design. The electromagnetic power loss density was calculated by:

$$p(\mathbf{r}) = \frac{1}{2}\sigma E(\mathbf{r})^2 \quad (3)$$

Where $\sigma$ is the electrical conductivity and $E(\mathbf{r})$ is the local electric field. For the antenna-only case simulation, the thickness of PE is set to be infinite to eliminate the FP resonance peaks. Note that the imaginary part of PE permittivity is slightly increased by fitting to better simulate the real case. Material properties are from published research articles.[53–56] We used an atomic force microscope (AFM) to measure the surface roughness of the $W_xV_{1-x}O_2$ side of a pressed $W_xV_{1-x}O_2$/PE film, which was peeled from an as-fabricated PEAC sample. The surface roughness $R_a$ is only 11 nm, which is roughly 1/1000 of the working wavelength. With such low surface roughness, we can conclude that the particles are tightly compressed and the optical properties of $W_xV_{1-x}O_2$ blocks are close to a solid block at wavelengths around ~10 μm.

The design of the dimensions of the $W_xV_{1-x}O_2$ block array was optimized in two stages: First, the optimization was carried out using numerical electromagnetic simulation with COMSOL Multiphysics; Second, the design was further optimized with experimental tests. At the numerical electromagnetic simulation stage, the fabrication feasibility of the metal template was considered and the following dimensions of $W_xV_{1-x}O_2$ blocks were chosen as the starting point: height $h$ = 1.5 μm, width $w$ = 2.6 μm. Next, a parameter scan of $h$ was performed with results shown in Figure S14A, showing that when h increases beyond 1.5 μm, the high-temperature state emissivity of the PEAC decreases, while the low-temperature state emissivity still increases. Thus, $h$ = 1.5 μm yields the highest emissivity tuning range. After the optimized value of h, a parameter scan of w was performed (Figure S14B), leading to the finding that the emissivity tuning range reaches maximum when $w$ = 3.6 μm. During the experimental tests of a PEAC, w was slighted adjusted to $w$ = 3 μm due to the following four issues: (1) Although the simulated optimal

Please cite this article in press as: Li et al., Printable, emissivity-adaptive and albedo-optimized covering for year-round energy saving, Joule (2023), https://doi.org/10.1016/j.joule.2023.09.011



$w$ = 3.6 μm promises the largest emissivity tuning range, it also leads to a high value of low-temperature emissivity ($\varepsilon_{sky}$ = 0.35), which works against the keeping-warm state at cold weather. (2) The holes on the imprinted polyethylene (PE) are too large when $w$ = 3.6 μm, causing structural instability during the $W_xV_{1-x}O_2$ particle deposition process as the walls between holes are too thin. (3) Larger w leads to higher solar absorptance as the $W_xV_{1-x}O_2$ particles cover too much area on the PEAC. (4) $W_xV_{1-x}O_2$ contributes to the majority of the cost, meaning that the cost of a PEAC scales with $w^2$. The final nominal values of dimensions are shown in Figure S5.

To demonstrate the optical enhancement by the optical antenna formed by $W_xV_{1-x}O_2$ blocks, we also compared the high temperature spectral emissivity with other three other geometries of $W_xV_{1-x}O_2$ arrays: cylinder shape, pyramid shape and hemisphere shape. The cylinder shape of structure units is commonly used for emissivity regulation. The pyramid and the hemisphere shapes were achieved using KOH etching and isotropic etching, respectively, instead of ICP etching on Si surface during step 3 of template fabrication (Figure S2). The bottom width of all shapes is set to be identical as that of the $W_xV_{1-x}O_2$ blocks since the same lithography pattern is used. Figure S13 shows that the blocks array, which has parallel faces of neighboring blocks, has the best optical enhancement in terms of emissivity, proving the mechanism of antenna resonance and importance of the "optical funneling" effect.

## Outdoor experiment setup

The model houses were 3D printed with white ABS filament by a 3D printer (Ultimaker 2+). With the reported thermal resistance of ABS 3D printing structure,[36] we adjusted the thickness of walls and roofs, as well as the 3D printing filling ratio to achieve a thermal resistance per unit area similar to that of real houses.[37] To simulate the solar absorption characteristics of real houses, the walls of the model houses were painted white, while the windows were painted black. Two temperature sensors are embedded in each model house structure to measure the roof temperature and indoor temperature, respectively.

The model houses were placed on a roof of a residential house in Berkeley, CA. To mitigate the influence of uneven ground surfaces, a foam board was utilized. Throughout the experiment, temperature readings were recorded by a Raspberry Pi, while detailed weather data were obtained from a nearby weather station.

## Thermal regulation simulation

We employed the energy-saving simulation method described in the published paper by Tang et al.[19] The stable surface temperature for a given material was calculated based on adiabatic approximation, assuming minimal heat transfer between the surface and the underlying structure. The climate parameters, such as air temperature ($T_a$), dew point temperature ($T_d$), wind speed ($v$), solar irradiance ($I$) and cloud coverage factor (CF) are obtained from TMY3 weather files available from the EnergyPlus database.[42] The sky-window emissivity of the PEAC used in the simulation was calculated from the experimental spectra of FTIR measurements, and the solar absorptance was determined by the UV-vis-IR spectrometer measurements. With this setup, the all-year-around temperature maps (Figure 4C) of the PEAC as well as all conventional materials with various static combinations of $A$ and $\varepsilon$ were calculated and compared.

We assumed that houses require heating when $T_s$ falls below a heating setpoint $T_{h,set}$ (22°C) and need cooling when $T_s$ exceeds a cooling setpoint $T_{c,set}$ (24°C).

Please cite this article in press as: Li et al., Printable, emissivity-adaptive and albedo-optimized covering for year-round energy saving, Joule (2023), https://doi.org/10.1016/j.joule.2023.09.011





Subsequently, the energy consumption on space heating, ventilation, and air conditioning (HVAC) was calculated with the temperature difference between $T_s$ and setpoints. Regressed coefficients relating our surface temperature results to reported EnergyPlus simulation[43] specific to each climate zone and house type were reported in previous work.[19] Note that the building thermal inertia were considered in the EnergyPlus simulation reported by Rosado et al..[43,57,58]

To demonstrate the energy efficiency advantage of a PEAC over conventional cool-roof materials, the difference in source energy consumption for thermal regulation ($\Delta E_{tr}$) between a PEAC (with best performing $A$ in the experimental range, Figure 4D) and a representative cool roof material ($A = 0.05$ and $\varepsilon_{sky} = 0.95$) was calculated in all 15 US climate zones. The results in the energy-saving calculations (Figure 1E, 5D, S17 and S18) are based on the pre-1980 single-family home, which is the dominant resident building type in the US[59] The heating, cooling, and total energy saving of a PEAC over a representative cool roof are plotted in Figure S19. As the solar absorptance increases, heating energy saving rises, indicating that the building benefits more from passive solar heating in cold weather and requires less energy in space heating to maintain a desirable temperature. However, higher solar absorption also offsets the cooling energy saving of a PEAC. As a result, an optimal solar absorptance that leads to maximum total energy saving exists and varies with different climate zones. The $\Delta E_{tr}$ results and corresponding optimal $A$ for all types of single-family homes are presented in Table S2. The energy-saving performance in hot climates is mainly limited by the lower limit of $A$. When $A$ is sufficiently low, the difference in cooling energy saving between the PEAC and the cool-roof material is as low as near-zero (Figure S19). Therefore, a PEAC may outperform conventional radiative coolers in all the climate zones in the US if an ideal solar absorptance range could be achieved (Figure S18).

The energy efficiency of a PEAC over commercial cool roofs in the outdoor temperature regulation experiment has been demonstrated following the same method. The temperature difference between the PEAC and the commercial cool roof was extracted from the 24 h experimental data, and the corresponding $E_{tr}$ was calculated with reported regressed coefficients.[19] The resulting $\Delta E_{tr}$ between the PEAC and the commercial cool roof material is 78.61 kJ/(m$^2$·day). Note that this summer daily $\Delta E_{tr}$ is lower than 1/365 of numerically simulated year-round $\Delta E_{tr}$ in Berkeley, CA, predicting that the PEAC should be more energy efficient in other seasons.

To evaluate the temperature regulation (thermal comfort) advantage of a PEAC in energy-poverty areas where heating and air conditioning are not used, a detailed numerical simulation was carried out with EnergyPlus. The simulation utilized a pre-1980 single-family house model, consisting of a living core zone, a garage, and an attic. The house model was generated from CBES[60] and San Francisco TMY3 weather data were used.[42] To simulate the condition in energy poverty area, the house is set to be unconditioned. The emissivity of the PEAC was set to be temperature-invariant outside of the atmospheric window, which leads to an underestimation of the thermal regulation performance of the PEAC, as the emissivity switching also exists outside of the sky window (Figure S6). After the calculation of the hour-by-hour indoor temperature throughout a year, the temperature regulation ability, or comfort potential, of the roof material is characterized by the dimensionless figure of merit (FOM) defined as

$$FOM = \frac{T_{set,avg} \int dt}{\int \left| T(t) - T_{set,avg} \right| dt} \quad (4)$$

Here $t$ is time and $T_{set,avg}$ is the average value of $T_{h,set}$ and $T_{c,set}$. Higher FOM indicates that the temperature $T(t)$ is more stable over time and temperature swing is narrower. We calculated the hourly temperature over a year for a house coated with a non-colored PEAC and a house coated with a common commercial roof ($A$ = 0.9 and $\varepsilon_{sky}$ = 0.9), respectively. Figure S20 shows that the house under the PEAC has higher FOM in all areas, which demonstrates the PEAC's temperature regulation ability for the free-floating cases.

## SUPPLEMENTAL INFORMATION

Supplemental information can be found online at https://doi.org/10.1016/j.joule.2023.09.011.

## ACKNOWLEDGMENTS

This work was supported by the U.S. Department of Energy, Office of Science, Office of Basic Energy Sciences, Materials Sciences and Engineering Division under contract no. DE-AC02-05CH11231 (Electronic Materials program). Work at the Molecular Foundry was supported by the U.S. Department of Energy, Office of Science, Office of Basic Energy Sciences under contract no. DE-AC02-05CH11231. The device design part of this work was supported by NSF grant no. ECCS-1953803. J. W. acknowledges the Bakar Prize.

## AUTHOR CONTRIBUTIONS

Jiachen Li, K.D., and J.W. conceived the general idea. Jiachen Li and K.D. designed the material. Jiachen Li and C.F. fabricated the material. Jiachen Li, K.D., T.Z., C.D., Jingang Li, C.P.G., J.J.U., and A.J. contributed to the spectral characterizations. Jiachen Li, K.D., T.Z., R.G., and J.W. performed the outdoor experiments. Jiachen Li, K.D., T.Z., Jingang Li, C.P.G., and J.Y. performed the numerical electromagnetic simulations. Jiachen Li, D.T., Y. X., and T.H. performed the other simulations. All authors discussed and analyzed the results. Jiachen Li, K.D., and J.W. wrote the manuscript with assistance from other authors. All authors reviewed and revised the manuscript.

## DECLARATION OF INTERESTS

A United States provisional patent application related to this work has been filed by J.W., Jiachen Li, and K.D.

Received: June 23, 2023
Revised: August 21, 2023
Accepted: September 25, 2023
Published: October 20, 2023

## REFERENCES

1. Orel, B., Gunde, M., and Krainer, A. (1993). Radiative cooling efficiency of white pigmented paints. Sol. Energy *50*, 477–482. https://doi.org/10.1016/0038-092X(93)90108-Z.

2. Lv, Y., Huang, A., Yang, J., Xu, J., and Yang, R. (2021). Improving cabin thermal environment of parked vehicles under direct sunlight using a daytime radiative cooling cover. Appl. Therm. Eng. *190*, 116776. https://doi.org/10.1016/j.applthermaleng.2021.116776.

3. Heo, S.Y., Lee, G.J., Kim, D.H., Kim, Y.J., Ishii, S., Kim, M.S., Seok, T.J., Lee, B.J., Lee, H., and Song, Y.M. (2020). A Janus emitter for passive heat release from enclosures. Sci. Adv. *6*, eabb1906. https://doi.org/10.1126/sciadv.abb1906.

4. Xiao, R., Hou, C., Yang, W., Su, Y., Li, Y., Zhang, Q., Gao, P., and Wang, H. (2019). Infrared-radiation-enhanced nanofiber membrane for sky radiative cooling of the human body. ACS Appl. Mater. Interfaces *11*, 44673–44681. https://doi.org/10.1021/acsami.9b13933.

5. Li, T., Zhai, Y., He, S., Gan, W., Wei, Z., Heidarinejad, M., Dalgo, D., Mi, R., Zhao, X., Song, J., et al. (2019). A radiative cooling structural material. Science *364*, 760–763. https://doi.org/10.1126/science.aau9101.

6. Mandal, J., Fu, Y., Overvig, A.C., Jia, M., Sun, K., Shi, N.N., Zhou, H., Xiao, X., Yu, N., and Yang, Y. (2018). Hierarchically porous polymer coatings for highly efficient passive daytime radiative cooling. Science *362*, 315–319. https://doi.org/10.1126/science.aat9513.

7. Zhai, H., Fan, D., and Li, Q. (2022). Scalable and paint-format colored coatings for passive radiative cooling. Sol. Energy Mater. Sol. Cell. *245*, 111853. https://doi.org/10.1016/j.solmat.2022.111853.

8. Li, X., Peoples, J., Huang, Z., Zhao, Z., Qiu, J., and Ruan, X. (2020). Full daytime sub-ambient radiative cooling in commercial-like paints with

high figure of merit. Cell Reports Physical Science *1*, 100221. https://doi.org/10.1016/j.xcrp.2020.100221.

9. Zeng, S., Pian, S., Su, M., Wang, Z., Wu, M., Liu, X., Chen, M., Xiang, Y., Wu, J., Zhang, M., et al. (2021). Hierarchical-morphology metafabric for scalable passive daytime radiative cooling. Science *373*, 692–696. https://doi.org/10.1126/science.abi5484.

10. Xie, B., Zhao, W., Luo, X., and Hu, R. (2023). Alignment engineering in thermal materials. Mater. Sci. Eng. R Rep. *154*, 100738. https://doi.org/10.1016/j.mser.2023.100738.

11. Zhai, Y., Ma, Y., David, S.N., Zhao, D., Lou, R., Tan, G., Yang, R., and Yin, X. (2017). Scalable-manufactured randomized glass-polymer hybrid metamaterial for daytime radiative cooling. Science *355*, 1062–1066. https://doi.org/10.1126/science.aai7899.

12. Raman, A.P., Anoma, M.A., Zhu, L., Rephaeli, E., and Fan, S. (2014). Passive radiative cooling below ambient air temperature under direct sunlight. Nature *515*, 540–544. https://doi.org/10.1038/nature13883.

13. Ulpiani, G., Ranzi, G., Shah, K.W., Feng, J., and Santamouris, M. (2020). On the energy modulation of daytime radiative coolers: A review on infrared emissivity dynamic switch against overcooling. Sol. Energy *209*, 278–301. https://doi.org/10.1016/j.solener.2020.08.077.

14. Zhao, X., Aili, A., Zhao, D., Xu, D., Yin, X., and Yang, R. (2022). Dynamic glazing with switchable solar reflectance for radiative cooling and solar heating. Cell Reports Physical Science *3*, 100853. https://doi.org/10.1016/j.xcrp.2022.100853.

15. Rao, Y., Dai, J., Sui, C., Lai, Y.T., Li, Z., Fang, H., Li, X., Li, W., and Hsu, P.C. (2021). Ultra-wideband transparent conductive electrode for electrochromic synergistic solar and radiative heat management. ACS Energy Lett. *6*, 3906–3915. https://doi.org/10.1021/acsenergylett.1c01486.

16. Li, X., Sun, B., Sui, C., Nandi, A., Fang, H., Peng, Y., Tan, G., and Hsu, P.C. (2020). Integration of daytime radiative cooling and solar heating for year-round energy saving in buildings. Nat. Commun. *11*, 6101. https://doi.org/10.1038/s41467-020-19790-x.

17. Xia, Z., Fang, Z., Zhang, Z., Shi, K., and Meng, Z. (2020). Easy way to achieve self-adaptive cooling of passive radiative materials. ACS Appl. Mater. Interfaces *12*, 27241–27248. https://doi.org/10.1021/acsami.0c05803.

18. Zhang, Q., Lv, Y., Wang, Y., Yu, S., Li, C., Ma, R., and Chen, Y. (2022). Temperature-dependent dual-mode thermal management device with net zero energy for year-round energy saving. Nat. Commun. *13*, 4874. https://doi.org/10.1038/s41467-022-32528-1.

19. Tang, K., Dong, K., Li, J., Gordon, M.P., Reichertz, F.G., Kim, H., Rho, Y., Wang, Q., Lin, C.-Y., Grigoropoulos, C.P., et al. (2021). Temperature-adaptive radiative coating for all-season household thermal regulation. Science *374*, 1504–1509. https://doi.org/10.1126/science.abf7136.

20. Wang, S., Jiang, T., Meng, Y., Yang, R., Tan, G., and Long, Y. (2021). Scalable thermochromic smart windows with passive radiative cooling regulation. Science *374*, 1501–1504. https://doi.org/10.1126/science.abg0291.

21. Wang, Z., Kim, S.K., and Hu, R. (2022). Self-switchable radiative cooling. Matter *5*, 780–782. https://doi.org/10.1016/j.matt.2022.01.018.

22. Morin, F.J. (1959). Oxides which show a metal-to-insulator transition at the Neel temperature. Phys. Rev. Lett. *3*, 34–36. https://doi.org/10.1103/PhysRevLett.3.34.

23. Wu, T.L., Whittaker, L., Banerjee, S., and Sambandamurthy, G. (2011). Temperature and voltage driven tunable metal-insulator transition in individual W x V 1− x O 2 nanowires. Phys. Rev. B *83*, 073101. https://doi.org/10.1103/PhysRevB.83.073101.

24. Kim, C., Shin, J.S., and Ozaki, H. (2007). Effect of W doping in metal–insulator transition material VO2 by tunnelling spectroscopy. J. Phys. Condens. Matter *19*, 096007. https://doi.org/10.1088/0953-8984/19/9/096007.

25. Lee, S., Hippalgaonkar, K., Yang, F., Hong, J., Ko, C., Suh, J., Liu, K., Wang, K., Urban, J.J., Zhang, X., et al. (2017). Anomalously low electronic thermal conductivity in metallic vanadium dioxide. Science *355*, 371–374. https://doi.org/10.1126/science.aag0410.

26. Batista, C., Ribeiro, R.M., and Teixeira, V. (2011). Synthesis and characterization of VO 2-based thermochromic thin films for energy-efficient windows. Nanoscale Res. Lett. *6*, 301–307. https://doi.org/10.1186/1556-276X-6-301.

27. Sardon, H., and Dove, A.P. (2018). Plastics recycling with a difference. Science *360*, 380–381. https://doi.org/10.1126/science.aat4997.

28. Barker, A.S., Jr., Verleur, H.W., and Guggenheim, H.J. (1966). Infrared optical properties of vanadium dioxide above and below the transition temperature. Phys. Rev. Lett. *17*, 1286–1289. https://doi.org/10.1103/PhysRevLett.17.1286.

29. Dong, K., Deng, Y., Wang, X., Tom, K.B., You, Z., and Yao, J. (2018). Subwavelength light confinement and enhancement enabled by dissipative dielectric nanostructures. Opt. Lett. *43* (8), 1826–1829. https://doi.org/10.1364/OL.43.001826.

30. Agassi, J. (1967). The Kirchhoff-Planck Radiation Law: Considering Kirchhoff's law as it was initially meant may help us understand the rise of quantum theory. Science *156*, 30–37. . https://doi.org/10.1126/science.156.3771.30.

31. Xi, W., Liu, Y., Zhao, W., Hu, R., and Luo, X. (2021). Colored radiative cooling: How to balance color display and radiative cooling performance. Int. J. Therm. Sci. *170*, 107172. https://doi.org/10.1016/j.ijthermalsci.2021.107172.

32. Xie, B., Liu, Y., Xi, W., and Hu, R. (2023). Colored radiative cooling: progress and prospects. Mater. Today Energy *34*, 101302. https://doi.org/10.1016/j.mtener.2023.101302.

33. Lozano, L.M., Hong, S., Huang, Y., Zandavi, H., El Aoud, Y.A., Tsurimaki, Y., Zhou, J., Xu, Y., Osgood, R.M., Chen, G., and Boriskina, S.V. (2019). Optical engineering of polymer materials and composites for simultaneous color and thermal management. Opt. Mater. Express *9* (5), 1990–2005. https://doi.org/10.1364/OME.9.001990.

34. Peng, Y., Fan, L., Jin, W., Ye, Y., Huang, Z., Zhai, S., Luo, X., Ma, Y., Tang, J., Zhou, J., et al. (2021). Coloured low-emissivity films for building envelopes for year-round energy savings. Nat. Sustain. *5*, 339–347. https://doi.org/10.1038/s41893-021-00836-x.

35. Wen, J., and Smith, T.F. (2002). Absorption of solar energy in a room. Sol. Energy *72*, 283–297. https://doi.org/10.1016/S0038-092X(01)00107-4.

36. Sonsalla, T., Moore, A.L., Meng, W.J., Radadia, A.D., and Weiss, L. (2018). 3-D printer settings effects on the thermal conductivity of acrylonitrile butadiene styrene (ABS). Polym. Test. *70*, 389–395. https://doi.org/10.1016/j.polymertesting.2018.07.018.

37. Treado, S.J. (1980). Thermal resistance measurements of a built-up roof system. Final report (No. PB-81-140063), National Engineering Lab.(NBS), Washington, DC (USA). https://www.osti.gov/biblio/5759462.

38. U.S. Energy Information Administration (2020). Annual Energy Review 2020. https://www.eia.gov/totalenergy/data/annual/.

39. U.S. Energy Information Administration (2015). 2015 Residential Energy Consumption Survey. https://www.eia.gov/consumption/residential/.

40. Moghaddaszadeh Ahrab, M.A., and Akbari, H. (2013). Hygrothermal behaviour of flat cool and standard roofs on residential and commercial buildings in North America. Build. Environ. *60*, 1–11. https://doi.org/10.1016/j.buildenv.2012.11.003.

41. Bludau, C., Zirkelbach, D., and Künzel, H.M. (2008). Condensation problems in cool roofs. In 11th international conference on durability of building materials and components.

42. U.S. Department of Energy's Building Technologies Office (2022). EnergyPlus. https://energyplus.net/.

43. Rosado, P.J., and Levinson, R. (2019). Potential benefits of cool walls on residential and commercial buildings across California and the United States: Conserving energy, saving money, and reducing emission of greenhouse gases and air pollutants. Energy Build. *199*, 588–607. https://doi.org/10.1016/j.enbuild.2019.02.028.

44. United States Environment Protection Agency. Greenhouse Gas Equivalencies Calculator. https://www.epa.gov/energy/greenhouse-gas-equivalencies-calculator

45. Chen, L., Huang, C., Xu, G., Miao, L., Shi, J., Zhou, J., and Xiao, X. (2012). Synthesis of thermochromic W-doped VO2 (M/R) nanopowders by a simple solution-based process. Journal of Nanomaterials *2012*, 1–8. https://doi.org/10.1155/2012/491051.

46. Liang, S., Shi, Q., Zhu, H., Peng, B., and Huang, W. (2016). One-step hydrothermal synthesis of W-doped VO2 (M) nanorods with a tunable phase-transition temperature for infrared smart windows. ACS Omega *1*, 1139–1148. https://doi.org/10.1021/acsomega.6b00221.

47. Yu, N., Genevet, P., Kats, M.A., Aieta, F., Tetienne, J.P., Capasso, F., and Gaburro, Z. (2011). Light propagation with phase discontinuities: generalized laws of reflection and refraction. Science *334*, 333–337. https://doi.org/10.1126/science.1210713.

48. Dong, K., Tseng, D., Li, J., Warkander, S., Yao, J., and Wu, J. (2022). Reducing temperature swing of space objects with temperature-adaptive solar or radiative coating. Cell Reports Physical Science *3*, 101066. https://doi.org/10.1016/j.xcrp.2022.101066.

49. Finckenor, M.M., and Dooling, D. (1999). Multilayer insulation material guidelines. (No. M-925). https://ntrs.nasa.gov/citations/19990047691.

50. Hatakenaka, R., Miyakita, T., Sugita, H., Saitoh, M., and Hirai, T. (2014). Development and testing of a zero stitch MLI blanket using plastic pins for space use. Cryogenics *64*, 121–134. https://doi.org/10.1016/j.cryogenics.2014.02.018.

51. Marinetti, S., and Cesaratto, P.G. (2012). Emissivity estimation for accurate quantitative thermography. NDT E Int. *51*, 127–134. https://doi.org/10.1016/j.ndteint.2012.06.001.

52. Cho, J.W., Lee, Y.J., Kim, J.H., Hu, R., Lee, E., and Kim, S.K. (2023). Directional Radiative Cooling via Exceptional Epsilon-Based Microcavities. ACS Nano *17*, 10442–10451. https://doi.org/10.1021/acsnano.3c01184.

53. Ordal, M.A., Bell, R.J., Alexander, R.W., Long, L.L., and Querry, M.R. (1985). Optical properties of fourteen metals in the infrared and far infrared: Al, Co, Cu, Au, Fe, Pb, Mo, Ni, Pd, Pt, Ag, Ti, V, and W. Appl. Opt. *24* (24), 4493–4499. https://doi.org/10.1364/AO.24.004493.

54. Dong, K., Hong, S., Deng, Y., Ma, H., Li, J., Wang, X., Yeo, J., Wang, L., Lou, S., Tom, K.B., et al. (2018). A Lithography-Free and Field-Programmable Photonic Metacanvas. Adv. Mater. *30*, 1703878. https://doi.org/10.1002/adma.201703878.

55. Qazilbash, M.M., Brehm, M., Andreev, G.O., Frenzel, A., Ho, P.C., Chae, B.G., Kim, B.J., Yun, S.J., Kim, H.T., Balatsky, A.V., et al. (2009). Infrared spectroscopy and nano-imaging of the insulator-to-metal transition in vanadium dioxide. Phys. Rev. B *79*, 075107. https://doi.org/10.1103/PhysRevB.79.075107.

56. Querry, M.R. (1998). Optical constants of minerals and other materials from the millimeter to the ultraviolet. https://apps.dtic.mil/sti/pdfs/ADA192210.pdf.

57. California Energy Commission (1998-2016). Building energy efficiency standards. http://www.energy.ca.gov/title24/.

58. Huang, J., Hanford, J., and Yang, F. (1999). Residential heating and cooling loads component analysis. https://p2infohouse.org/ref/36/35857.pdf.

59. Energy Information Administration (2015). Forms EIA-457A and EIA-457C of the 2015 Residential Energy Consumption Survey, Table HC2.1: Structural and Geographic Characteristics of U.S. Homes by Housing Unit Type. https://www.eia.gov/consumption/residential/data/2015/hc/php/hc2.1.php.

60. Lawrence Berkeley National Laboratory. Commercial Building Energy Saver. https://cbes.lbl.gov/

## Supplemental Information

### Supplemental Figures

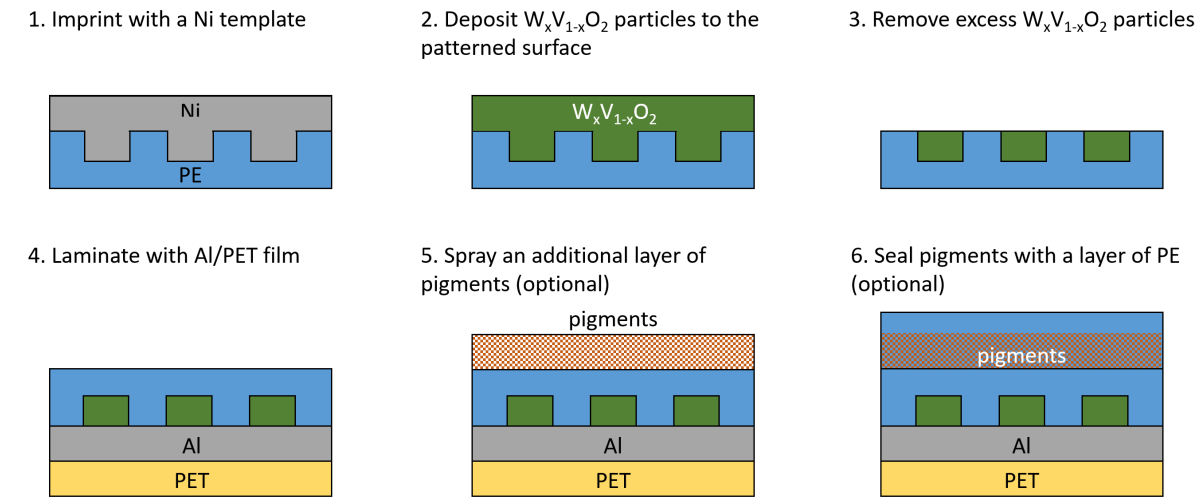


**Figure S1. Schematics for fabrication of PEAC.**

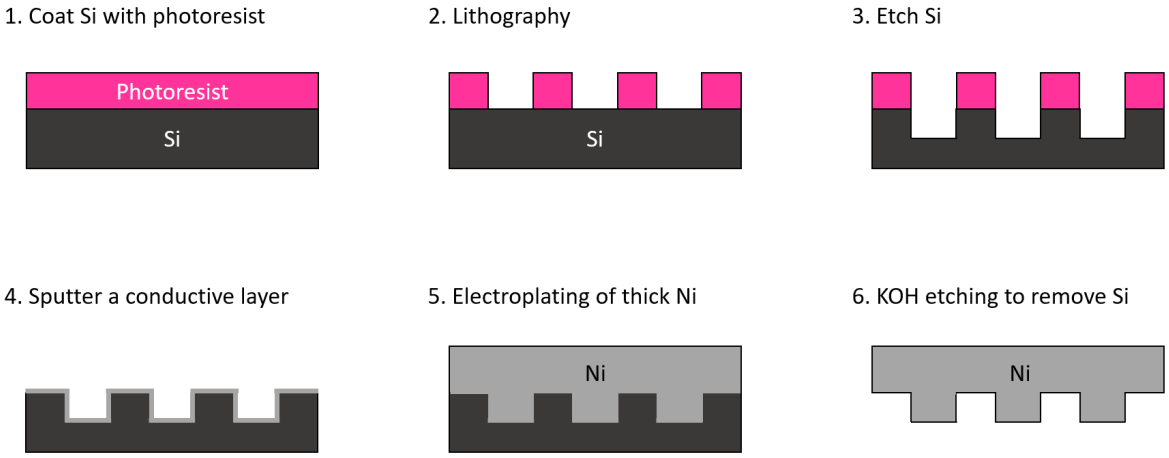


**Figure S2. Schematics for fabrication of reusable templates.**

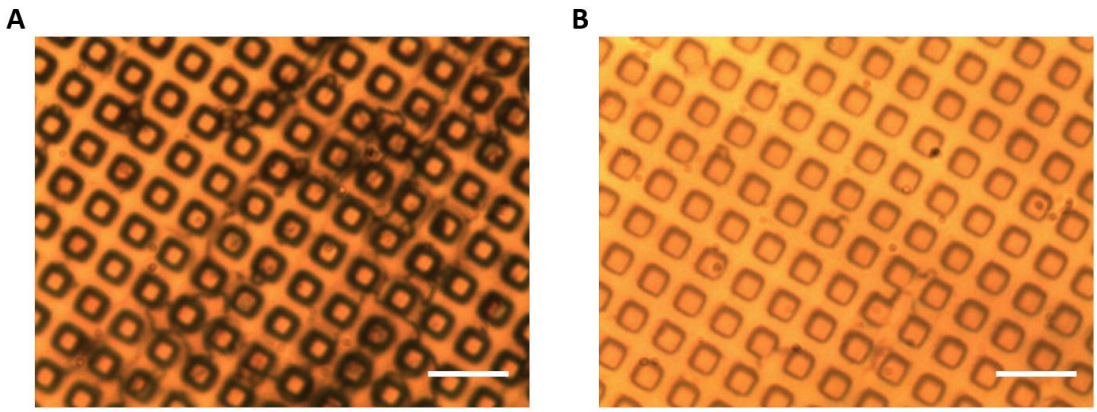


**Figure S3. Microscopic images of an imprinting template (A) and an imprinted PE film (B).** Scale bar: 10 μm.

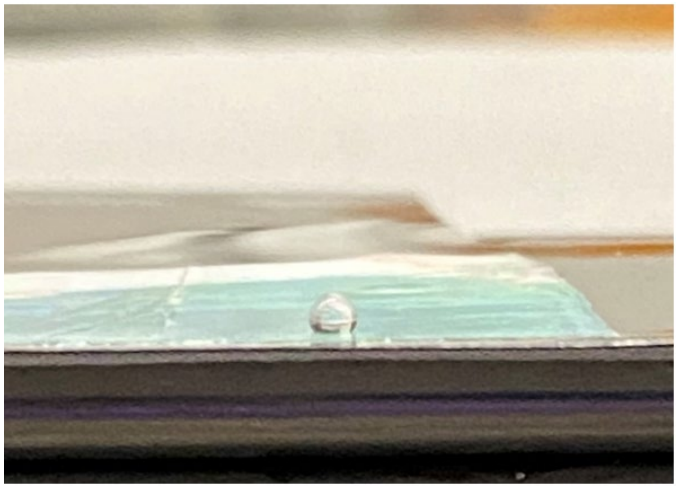

**Figure S4. A photo showing the hydrophobicity of PEAC surface.**

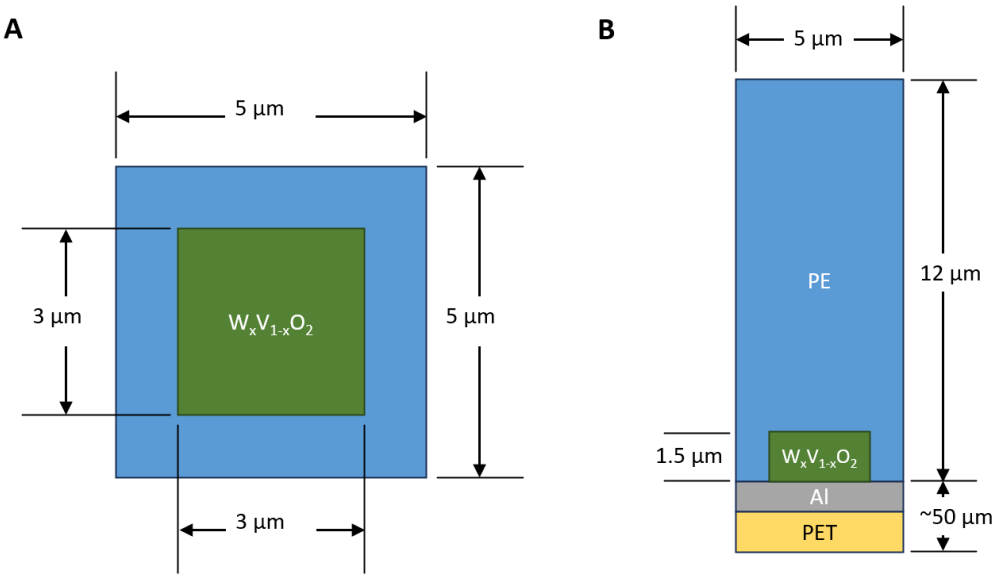


**Figure S5. Nominal dimensions of the $W_xV_{1-x}O_2$ antenna array.** (A) and (B) are top and side view of a unit cell, respectively.

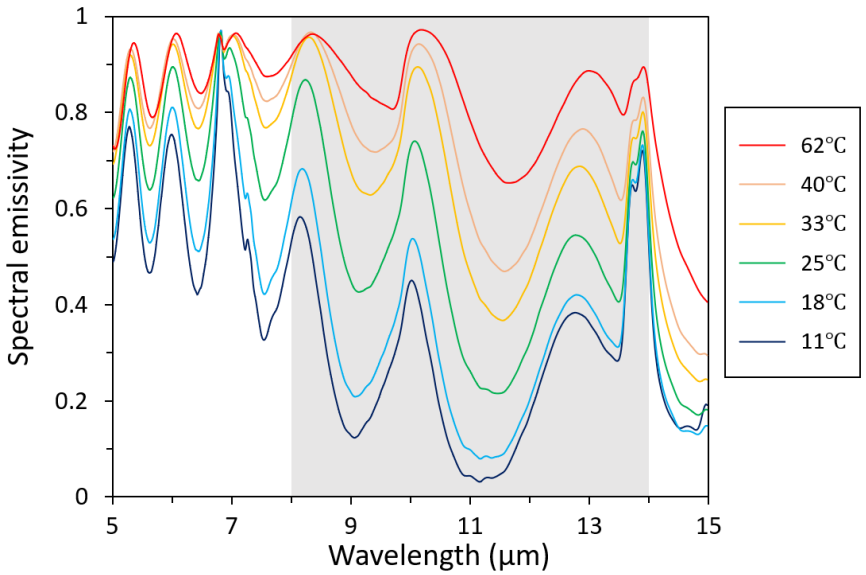


**Figure S6. Temperature-dependent infrared spectra of PEAC made with $W_xV_{1-x}O_2$ ($x$=2%).** The atmospheric window is shown as a shaded area.

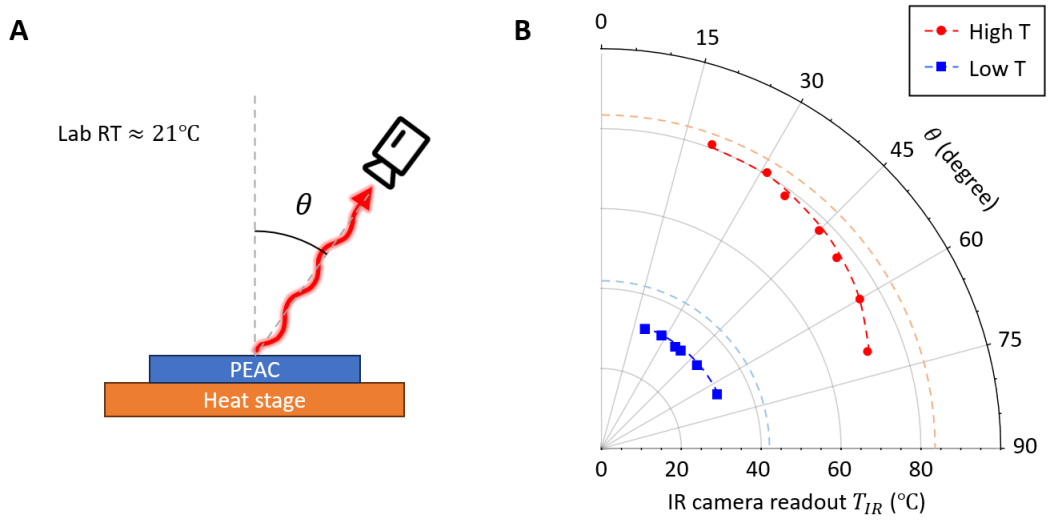


**Figure S7. The angular-dependent IR camera measurement.**
(A) A schematic of the experiment setup. A $VO_2$ sample with ~67°C was used to ensure a good contrast to the ambient temperature thermal emission background.
(B) The result of the angular-dependent IR camera measurement.

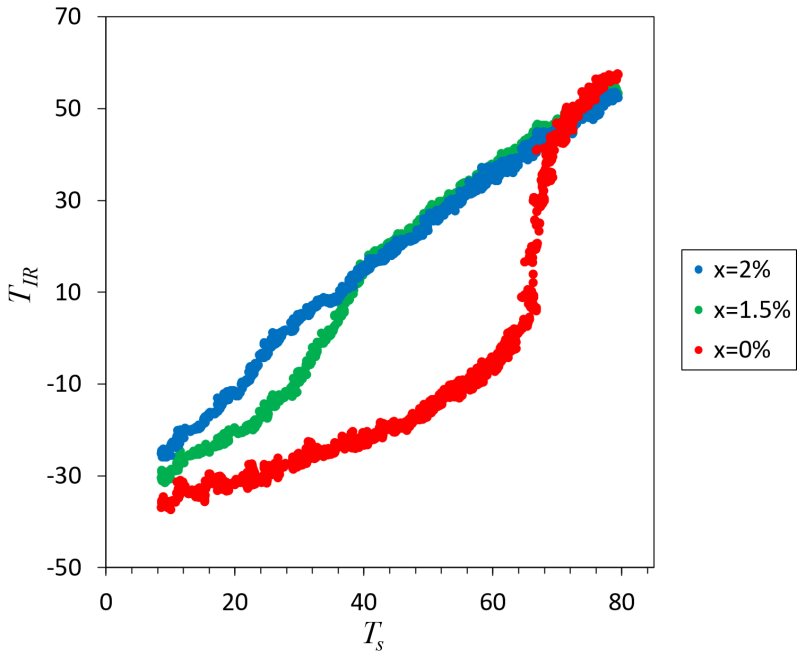


**Figure S8. Infrared camera readout shows the tunability of $T_{MIT}$ with different $W_xV_{1-x}O_2$.**

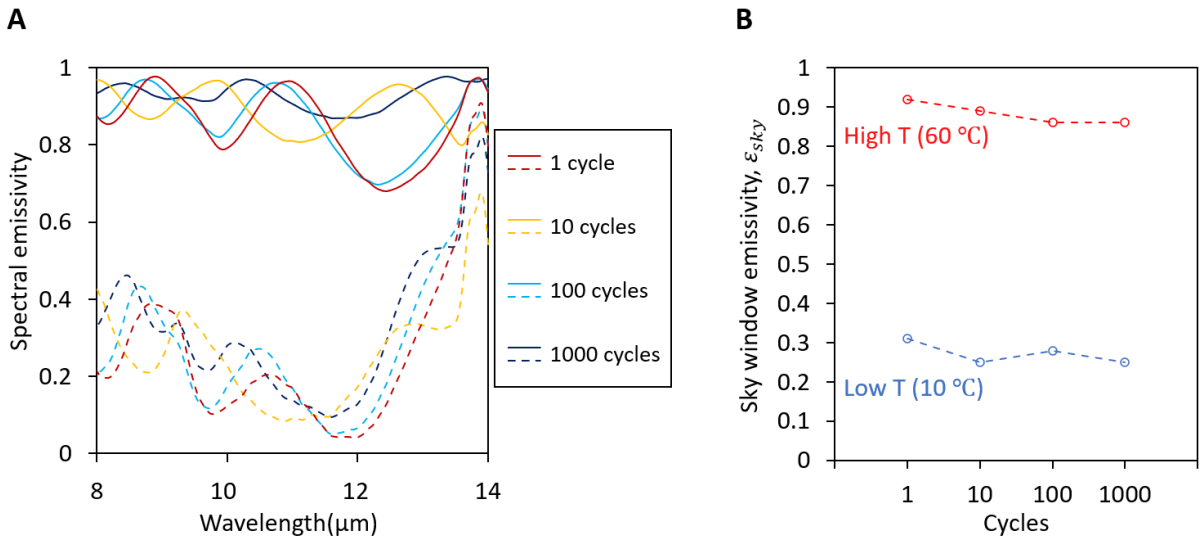


**Figure S9. Durability test of PEAC.**
(A) FTIR spectra of PEAC after given numbers of heating/cooling cycles. Solid lines represent high temperature (60 °C) data, while dashed lines represent low temperature (10 °C) data.
(B) Sky-window emissivity of PEAC after given number of heating/cooling cycles. The difference in spectra is mainly caused by the thickness variation of the PE layer.

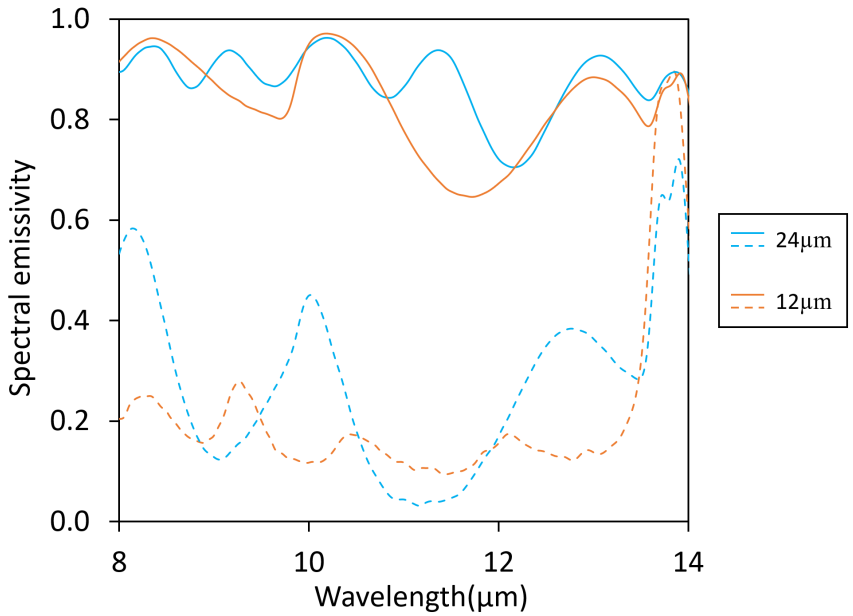


**Figure S10. Experimental FTIR spectra of PEAC with different PE thickness.** Solid lines represent high temperature (60 °C) data, while dashed lines represent low temperature (10 °C) data.

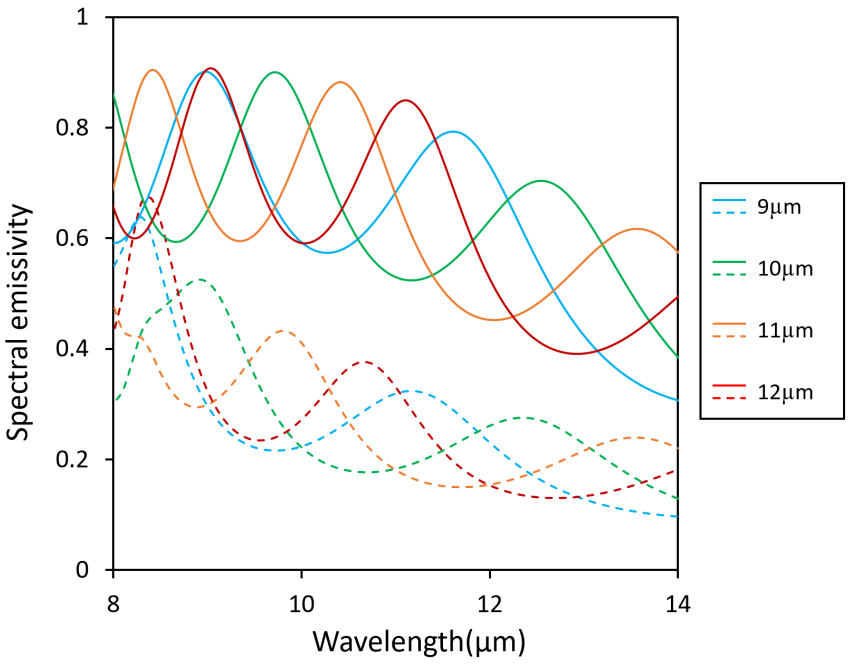


**Figure S11. Numerically simulated spectral emissivity for PEAC with different PE thickness.** Solid lines represent high temperature data, while dashed lines represent low temperature data.

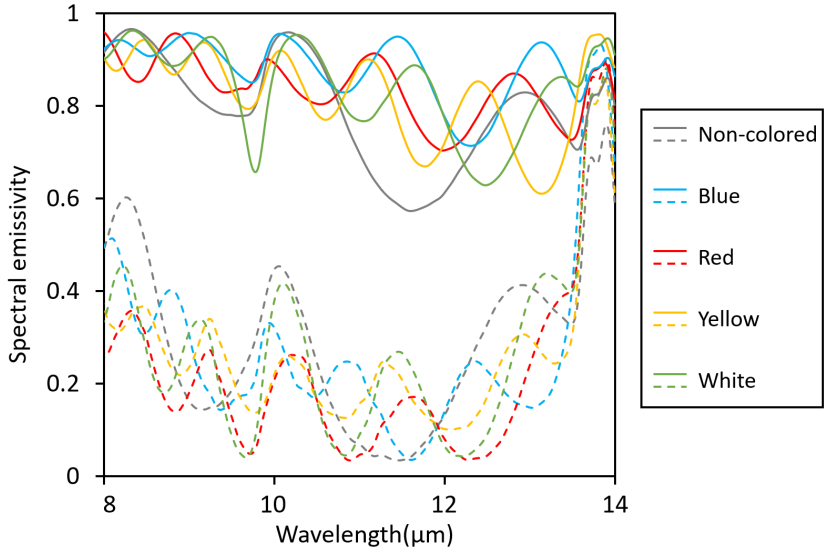


**Figure S12. Experimental FTIR spectra of PEAC with different colors.** Solid lines represent high temperature data, while dashed lines represent low temperature data. The insensitivity of emissivity switch to the addition of pigments is justified.

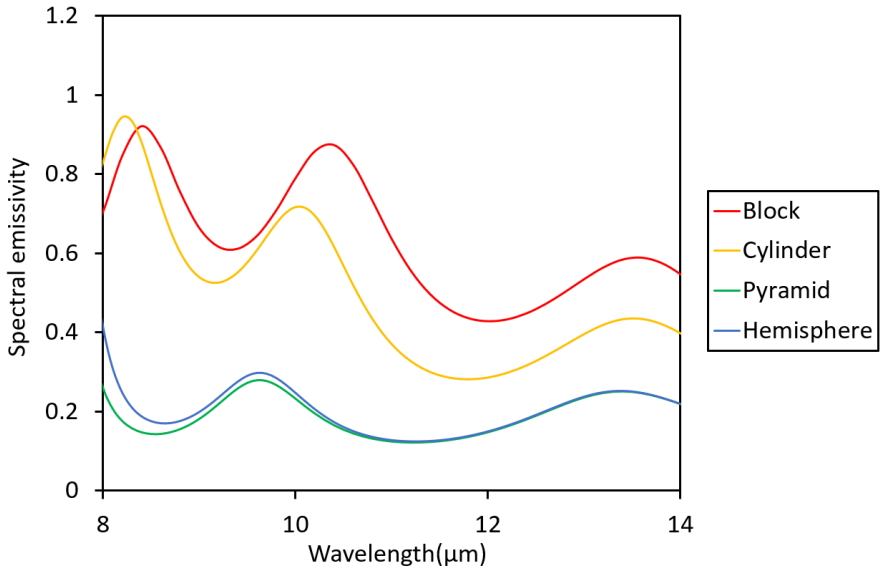


**Figure S13. Numerically simulated high-temperature state spectral emissivity for different shapes of $W_xV_{1-x}O_2$ arrays.**

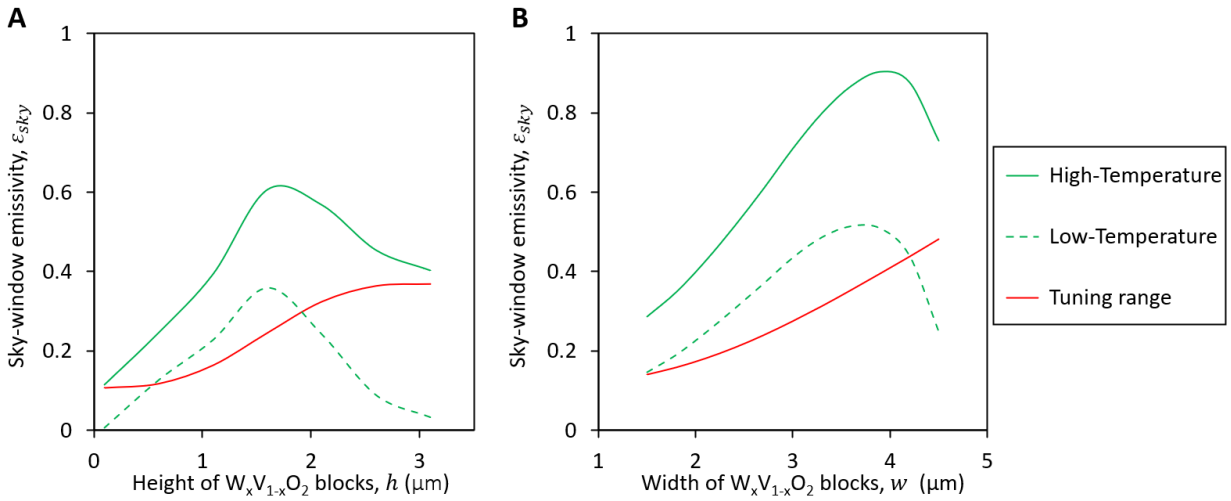


**Figure S14. Optimization of dimensions of the $W_xV_{1-x}O_2$ block array.**
(A) Parameter scan result of height of $W_xV_{1-x}O_2$ blocks ($h$).
(B) Parameter scan result of width of $W_xV_{1-x}O_2$ blocks ($w$).

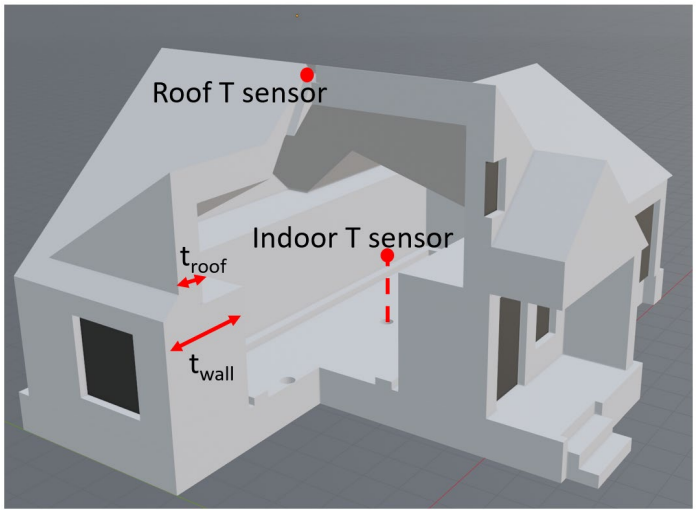


**Figure S15. Design of the model houses for outdoor experiments.**

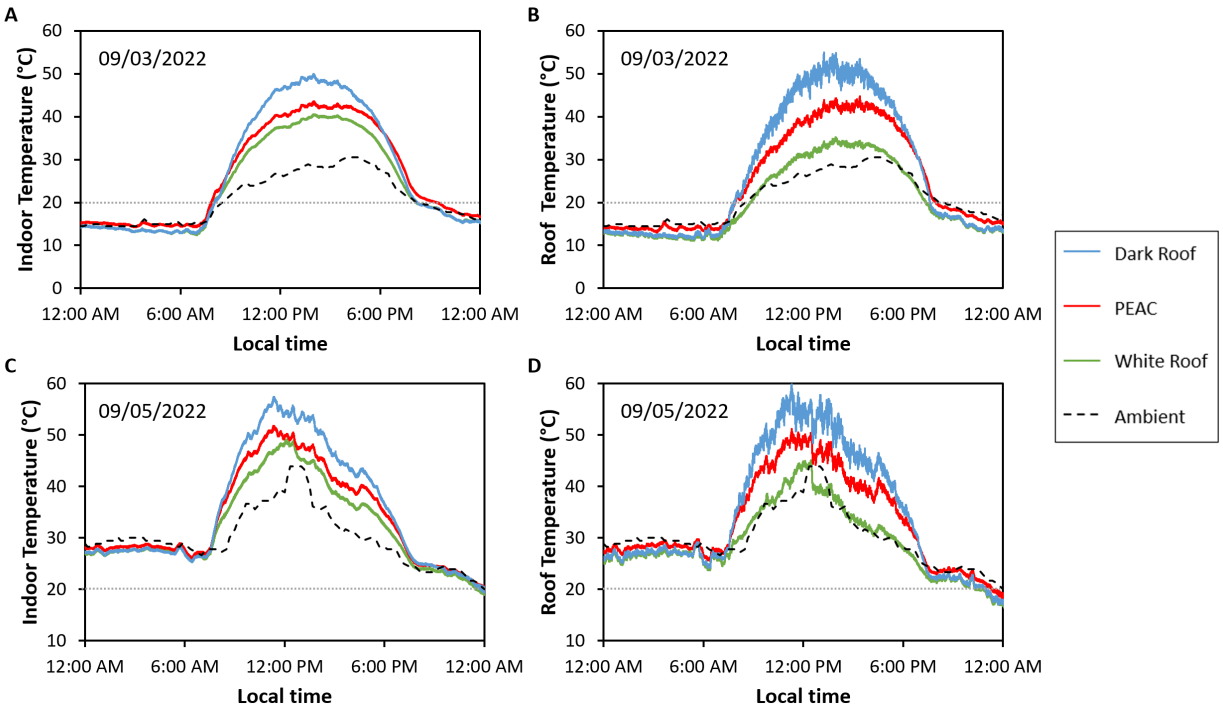


**Figure S16. Outdoor experiment results on two cloudless days in Berkeley, CA.** The maximum global horizontal solar irradiance was 901 W/m$^2$ (September 3rd, 2022) and 871 W/m$^2$ (September 5th, 2022).
(A), (C) Temperature data from the sensors inside the model houses.
(B), (D) Temperature data from the sensors integrated in the roof of the model houses. The gray dotted lines show the $T_{MIT}$ of PEAC.

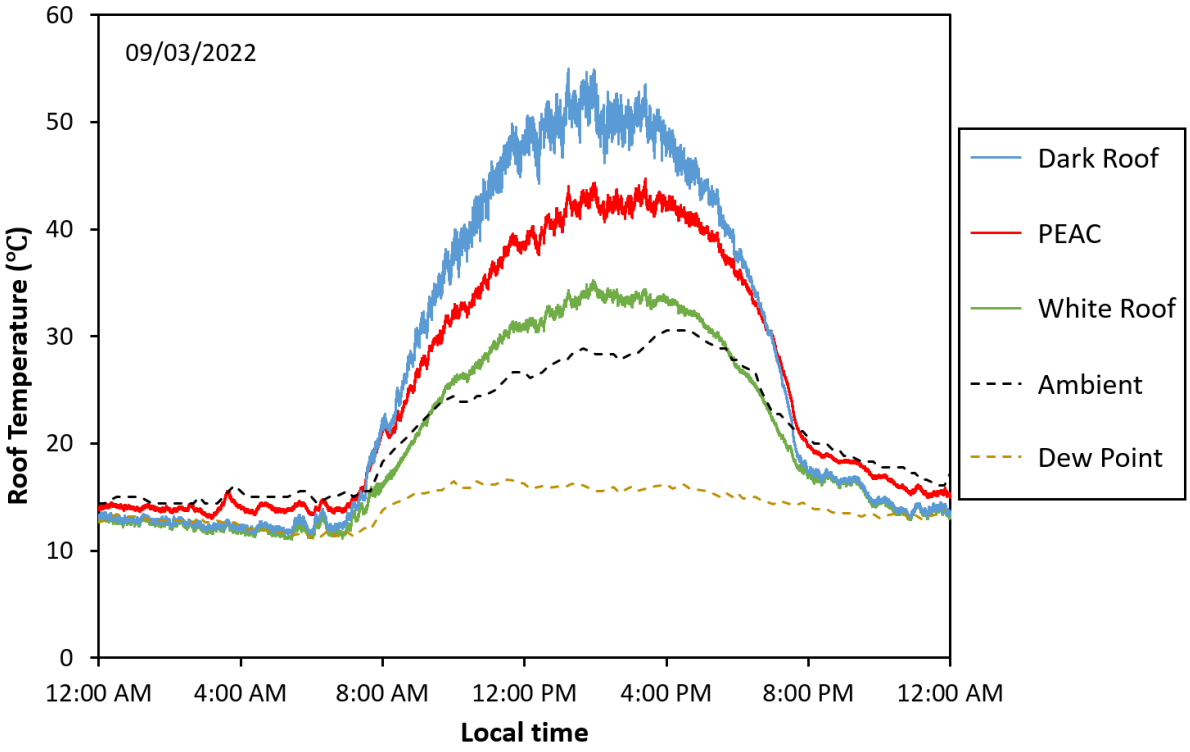


**Figure S17. Experimental roof temperatures covered by different coatings on Sep 3rd, 2022.** Both the white and dark roofs were over-cooled to the dew point during the nighttime.

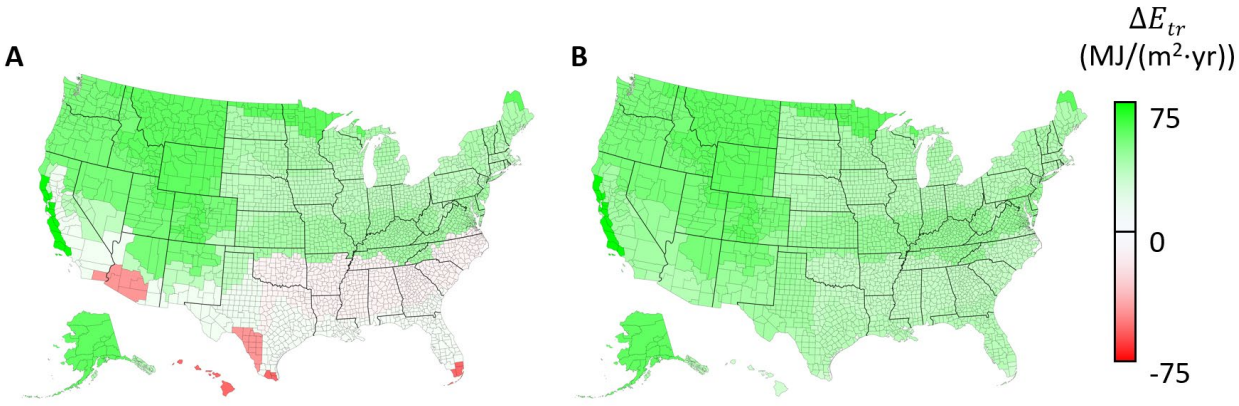


**Figure S18. Energy saving map with different solar absorptance range.**
(A) Energy saving map with our experimental PEAC solar absorptance range.
(B) Energy saving map with ideal PEAC solar absorptance range (0 to 1).

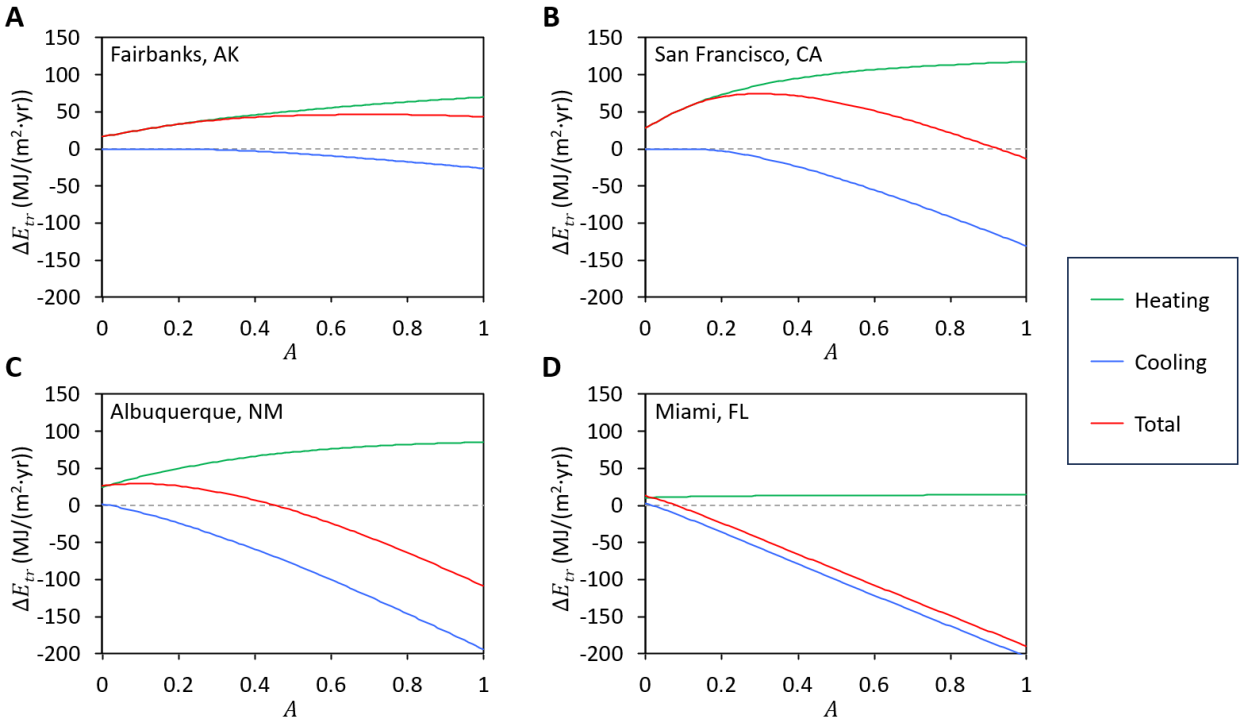


**Figure S19. Energy saving of PEAC compared to a representative cool-roof material, as a function of solar absorptance $A$.**

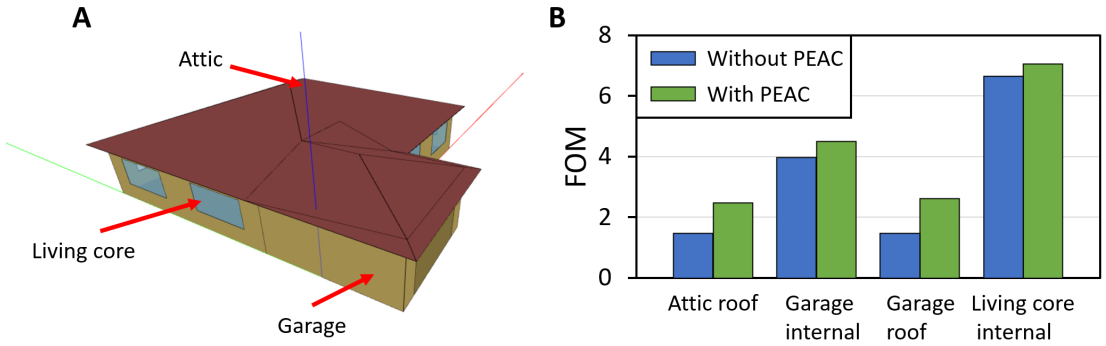


**Figure S20. Simulation of temperature regulation in energy poverty areas.**
(A) Setup of the house model for EnergyPlus simulation.
(B) Dimensionless FOM of temperature regulation in energy poverty areas.

**Supplemental Tables**

| Reference | Representative Materials | Working principle | $\Delta\varepsilon_{sky}$ | Scalability | Low cost | Robustness | Albedo-optimization | Mechanical flexibility | Zero power consumption |
|---|---|---|---|---|---|---|---|---|---|
| This work | $VO_2$/PE/Al | Optical antenna array | 0.6 | √ | √ | √ | √ | √ | √ |
| [S1] | $VO_2$/PMMA/ITO glass | Fabry-Perot resonator | 0.4 | √ | | | √ | | √ |
| [S2] | $VO_2$/$BaF_2$/Ag | Fabry-Perot resonator | 0.7 | | | | | √ | √ |
| [S3] | DOP-modified-PMP/TiO2, Nano-Cr/Al | Temperature-activated bimorph | 0.89 | √ | | | √ | √ | √ |
| [S4] | Silica particles/PP/, Ag/Cu | Temperature shape memory effect | 0.19 | √ | | | √ | | √ |
| [S5] | PDMS/Ag, Zn/Cu | Motor driven | 0.8 | √ | √ | | √ | √ | |
| [S6] | PE/Au/graphene | Electrodeposition | 0.82 | | | √ | √ | √ | |
| [S7] | Electrolyte/ITO glass | Electrodeposition | 0.8 | √ | | √ | √ | | |

**Table S1. Comparison of representative temperature-adaptive radiative cooling technologies.**

| Material | Vendor/brand | Unit Price | Amount per unit area of PEAC | Cost |
|---|---|---|---|---|
| $W_xV_{1-x}O_2$ | Hongwu International Group Ltd. | \$2.63/g | 0.23 g/sqft | \$0.60/sqft |
| PE | S. C. Johnson & Son | \$5/roll (11.5 inch ×104.4 ft) | 0.01 roll/sqft | \$0.05/sqft |
| Al foil (substrate 1) | Rhino Aluminum | \$40/roll (18 inch ×500 ft) | 0.0013 roll/sqft | \$0.05/sqft |
| Al/PET film (substrate 2) | McMaster-Carr | \$10.52/roll (27 inch ×12 ft) | 0.037 roll/sqft | \$0.39/sqft |
| Electricity cost (10 kW power usage, 100 m/hour speed, U.S average rate) | | | | \$0.007/sqft |
| Total cost (substrate 1) | | | | \$0.70/sqft |
| Total cost (substrate 2) | | | | \$1.04/sqft |

**Table S2. Detailed analysis of cost of PEAC in the lab stage.**

| Climate Zone | City | Pre-1980 | | 1980-1999 | | After-1999 | |
|---|---|---|---|---|---|---|---|
| | | $\Delta E_{tr}$(MJ/m$^2$/yr) | $A$ | $\Delta E_{tr}$(MJ/m$^2$/yr) | $A$ | $\Delta E_{tr}$(MJ/m$^2$/yr) | $A$ |
| 1A | Miami, FL | -44.40 | 0.30 | -15.94 | 0.30 | -12.19 | 0.30 |
| 2A | Houston, TX | 1.94 | 0.30 | 9.11 | 0.30 | 11.06 | 0.30 |
| 2B | Phoenix, AZ | -30.59 | 0.30 | -1.31 | 0.30 | -3.54 | 0.30 |
| 3A | Memphis, TN | -2.74 | 0.30 | 3.97 | 0.30 | 4.04 | 0.30 |
| 3B | El Paso, TX | 3.71 | 0.30 | 19.79 | 0.30 | 16.64 | 0.30 |
| 3C | San Francisco, CA | 74.29 | 0.30 | 61.47 | 0.43 | 39.10 | 0.42 |
| 4A | Baltimore, MD | 24.84 | 0.30 | 16.25 | 0.30 | 12.83 | 0.31 |
| 4B | Albuquerque, NM | 18.22 | 0.30 | 25.60 | 0.30 | 25.82 | 0.31 |
| 4C | Seattle, WA | 38.02 | 0.51 | 28.86 | 0.68 | 21.38 | 0.68 |
| 5A | Peoria, IL | 17.73 | 0.30 | 14.11 | 0.30 | 12.00 | 0.30 |
| 5B | Boise, ID | 39.19 | 0.33 | 27.06 | 0.50 | 28.58 | 0.62 |
| 6A | Burlington, VT | 22.95 | 0.39 | 23.67 | 0.56 | 18.04 | 0.54 |
| 6B | Helena, MT | 46.62 | 0.37 | 29.51 | 0.55 | 28.93 | 0.64 |
| 7 | Duluth, MN | 47.40 | 0.58 | 34.49 | 0.70 | 27.36 | 0.70 |
| 8 | Fairbanks, AK | 46.36 | 0.70 | 30.72 | 0.70 | 29.12 | 0.70 |
| CA climate zone 3 | Berkeley, CA | 53.82 | 0.30 | 47.22 | 0.35 | 30.00 | 0.33 |

**Table S3. Energy saving $\Delta E_{tr}$ and corresponding optimal solar absorptance $A$ for single-family homes in the U.S., calculated from numerical simulation with real climate data.** The solar absorptance values used in the simulation were within the experimental solar absorptance range (0.3 to 0.7).

**Supplemental References**


S1. Wang, S., Jiang, T., Meng, Y., Yang, R., Tan, G., & Long, Y. (2021). Scalable thermochromic smart windows with passive radiative cooling regulation. Science, 374(6574), 1501-1504. <https://doi.org/10.1126/science.abg0291>.

S2. Tang, K., Dong, K., Li, J., Gordon, M. P., Reichertz, F. G., Kim, H., Rho, Y., Wang, Q., Lin, C-Y., Grigoropoloulos, C.P., et al. (2021). Temperature-adaptive radiative coating for all-season household thermal regulation. Science, 374(6574), 1504-1509. <https://doi.org/10.1126/science.abf7136>.

S3. Zhang, Q., Lv, Y., Wang, Y., Yu, S., Li, C., Ma, R., & Chen, Y. (2022). Temperature-dependent dual-mode thermal management device with net zero energy for year-round energy saving. Nature communications, 13(1), 4874. <https://doi.org/10.1038/s41467-022-32528-1>.

S4. Xia, Z., Fang, Z., Zhang, Z., Shi, K., & Meng, Z. (2020). Easy way to achieve self-adaptive cooling of passive radiative materials. ACS applied materials & interfaces, 12(24), 27241-27248. <https://doi.org/10.1021/acsami.0c05803>.

S5. Li, X., Sun, B., Sui, C., Nandi, A., Fang, H., Peng, Y., Tan, G., & Hsu, P. C. (2020). Integration of daytime radiative cooling and solar heating for year-round energy saving in buildings. Nature communications, 11(1), 6101. < https://doi.org/10.1038/s41467-020-19790-x>.

S6. Rao, Y., Dai, J., Sui, C., Lai, Y.T., Li, Z., Fang, H., Li, X., Li, W. and Hsu, P.C. (2021). Ultra-wideband transparent conductive electrode for electrochromic synergistic solar and radiative heat management. *ACS Energy Letters*, *6*(11), 3906-3915. <https://doi.org/10.1021/acsenergylett.1c01486>.

S7. Zhao, X., Aili, A., Zhao, D., Xu, D., Yin, X., & Yang, R. (2022). Dynamic glazing with switchable solar reflectance for radiative cooling and solar heating. Cell Reports Physical Science, 3(4), 100853. <https://doi.org/10.1016/j.xcrp.2022.100853>.